Electronic supplementary information (ESI) for

Triphenylamine-ethylenedioxythiophene copolymers for perovskite solar cells: impact of substituent type and alternation

Lifei He,‡[a] Yuyan Zhang,‡[a] Bing Zhang,[a] Yanfei Mu,[b] Niansheng Xu,*[a] Yaohang Cai,*[a] Yi Yuan,[a] Jing Zhang,[a] Min Zhang[b] and Peng Wang*[a]

[a]*State Key Laboratory of Silicon and Advanced Semiconductor Materials, Department of Chemistry, Zhejiang University, Hangzhou 310058, China.*

[b]*Institute for New Energy Materials and Low Carbon Technologies, Tianjin University of Technology, Tianjin, 300384, China*

* Corresponding authors.

E-mail addresses: nshxu@zju.edu.cn, caiyh@zju.edu.cn, pw2015@zju.edu.cn.

1 Experimental section

1.1 Materials

Diphenylamine (98%, Energy Chemical), tris(dibenzylideneacetone)dipalladium ($Pd_2(dba)_3$, 98%, Energy Chemical), tri-*tert*-butylphosphine tetrafluoroborate ($HP(t\text{-}Bu)_3BF_4$, 98%, Energy Chemical), sodium *tert*-butoxide (NaO(*t*-Bu), 98%, Energy Chemical), *N*-bromosuccinimide (NBS, 98%, Energy Chemical), sodium sulfite (≥ 97%, Energy Chemical), 2-(2,3-dihydrothieno[3,4-*b*][1,4]dioxin-5-yl)-4,4,5,5-tetramethyl-1,3,2-dioxaborolane (98%, Aladdin), palladium diacetate ($Pd(OAc)_2$, 99%, Energy Chemical), 2-dicyclohexylphosphino-2',6'-dimethoxybiphenyl (SPhos, 98%, Energy Chemical), potassium phosphate (K_3PO_4, 99%, Energy Chemical), 3,4-ethylenedioxythiophene (EDOT, 98%, Bidepharm), tricyclohexylphosphonium tetrafluoroborate ($HP(Cy)_3BF_4$, 98%, Energy Chemical), potassium carbonate (K_2CO_3, 99%, Energy Chemical), 1-ethyl-3-methylimidazolium bis(trifluoromethanesulfonyl)imide (EMITFSI, 98%, Energy Chemical), ferrocene (97%, Aldrich), PEDOT:PSS (AI 4083, Heraeus® Clevios), benzocyclobutene (BCB, 98%, Energy Chemical), lead(II) iodide(PbI_2, 99.99%, TCI), rubidium chloride (RbCl, 99.9%, 3A), formamidinium iodide (FAI, 99.0%, Greatcell Solar), methylamine hydrochloride (MACl, 98%, TCI), triphenylmethane-4,4',4''-triisocyanate (TTI, 20% solution in chlorobenzene, Aladdin), polystyrene (PS, typical M_w ~ 280,000, Sigma-Aldrich), tin(IV) dioxide (SnO_2, 15% hydrocolloid dispersion, Alfa Aesar), 4-*tert*-butylpyridine (TBP, 96%, Sigma-Aldrich), and $N^2,N^2,N^{2'},N^{2'},N^7,N^7,N^{7'},N^{7'}$-octakis(4-methoxyphenyl)-9,9'-spirobi[fluorene]-2,2',7,7'-tetraamine (spiro-OMeTAD, 99.8%, Xi'an Polymer Light Technology Corp.) were purchased from commercial suppliers and used without further purification. Solvents including 1,4-dioxane (99%, Energy Chemical), *N*,*N*-dimethylacetamide (DMAc, 99.8%, extra dry, with molecular sieves, Water≤50 ppm, Energy Chemical), toluene (≥ 99.5%, Sinopharm Chemical Reagent Co., Ltd.), petroleum ether (boiling range 60–90 °C, Energy Chemical), tetrahydrofuran (THF, ≥ 99%, Sinopharm Chemical Reagent Co., Ltd.), methanol (≥ 99.5%, Sinopharm Chemical Reagent Co., Ltd.), deuterated tetrahydrofuran (THF-d_8, 99%, J&K Scientific), acetonitrile (MeCN, ≥ 99.9%, Energy Chemical), acetone (≥ 99.5%, Sinopharm Chemical Reagent Co., Ltd), ethanol (99.7%, Aladdin), chlorobenzene (99.8%, Acros Organics), dimethyl sulfoxide (DMSO, 99.9%, Sigma-Aldrich), *N*,*N*-dimethylformamide (DMF, Water ≤ 30 ppm, 99.9%, Energy Chemical), and 2-propanol (IPA, 99.5%, Sigma-Aldrich) were also acquired from commercial sources and employed without further purification. Deionized water with resistivity greater than 18 MΩ cm was provided by a UPR-II-10T Ultrapure water system (ULUPURE). The preparations of poly[bis(4-phenyl)(2,4,6-trimethylphenyl)amine] (PTAA, M_n = 19.3 kDa, PDI = 1.8),[1] 1-bromo-4-(2-octyldodecyloxy)benzene,[2] *N*,*N*-bis(4-bromophenyl)-2,4,6-trimethylaniline,[3] and 4-(*tert*-butyl)pyridinium 1,1,2,2,3,3-hexafluoropropane-1,3-disulfonimide (TBPH-HFSI)[4] followed the literature procedures.

1.2 General instrumentation

Melting point determinations were conducted using a WRS-1B digital melting point apparatus (INESA). ^1H and ^{13}C nuclear magnetic resonance (NMR) spectra were acquired on an AVANCE III 400 NMR spectrometer

(Bruker). All chemical shifts were referenced to THF-d_8. High resolution mass spectra (HR-MS) were recorded on a 6545 LC/Q-TOF system (Agilent). Attenuated total reflection-Fourier transform infrared (ATR-FTIR) spectroscopy measurements were carried out utilizing a Thermo Scientific™ Nicolet™ iS10 FTIR spectrometer. Ultraviolet-visible (UV-vis) absorption spectra were acquired with a Cary 8454 spectrophotometer (Agilent Technologies). Carbon, hydrogen, and nitrogen content analyses were conducted employing a Vario Micro cube element analyzer (Elementar Analysensysteme GmbH). High temperature gel permeation chromatography (HT-GPC) measurements were performed using a PL-GPC220 instrument (Polymer Laboratories Ltd.), with 1,2,4-trichlorobenzene as the eluent. Differential scanning calorimetry measurements were executed on a DSC Q100 V9.7 Build 291 instrument (TA) under a flowing nitrogen atmosphere, employing a heating rate of 10 ^{o}C min^{-1}. Impedance spectra were examined using an Autolab PGSTAT302N electrochemical workstation in the dark, covering a wide frequency range (10 Hz–3 MHz) with a small perturbation of 20 mV. Atom force microscopy measurements were conducted by a Park NX10 microscope (Park Systems). Top-view surface morphologies of thin films were imaged using a SU-70 field emission scanning electron microscope (Hitachi). Fluorescence optical microscopy images were recorded employing an ECLIPSE Ti-U system (Nikon).

1.3 Synthetical procedures

1.3.1 4-((2-Octyldodecyl)oxy)-*N*,*N*-diphenylaniline (TPAOOD)

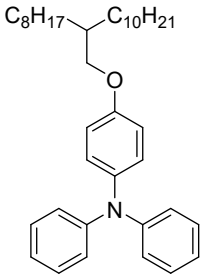

To a round-bottom flask were added diphenylamine (3.4 g, 20 mmol), 1-bromo-4-(2-octyldodecyloxy)benzene (10.8 g, 24 mmol), $Pd_2(dba)_3$ (458 mg, 0.5 mmol), HP(*t*-Bu)$_3$BF$_4$ (290 mg, 1.0 mmol), NaO(*t*-Bu) (5.8 g, 60 mmol), and toluene (60 mL). The flask was subjected to three cycles of evacuation and argon purging. The reaction mixture was then refluxed for 12 hours. After cooling to room temperature, the mixture was filtered through a Kieselguhr pad. The filtrate was concentrated under reduced pressure, and the residue was purified by column chromatography on neutral alumina (petroleum ether, 60–90 °C) to afford the desired product as a colorless oil (9.8 g, 90% yield). ^{1}H NMR (400 MHz, THF-d_8) δ: 7.05 (t, J = 6.3 Hz, 4H), 6.88 (m, 6H), 6.82–6.67 (m, 4H), 3.73 (d, J = 4.3 Hz, 2H), 1.63–1.71 (m, 1H), 1.37–1.10 (m, 32H), and 0.78 (t, J = 5.1 Hz, 6H) ppm. ^{13}C NMR (100 MHz, THF-d_8) δ: 157.40, 149.48, 141.66, 129.92, 128.34, 123.76, 122.66, 116.26, 71.70, 39.34, 33.04, 32.56, 31.18, 30.81, 30.77, 30.73, 30.47, 28.01, 23.72, and 14.61 ppm. HR-MS *m*/*z* calcd. for $[M+H]^+$: 542.4356. Found: 542.4345. ATR-FTIR (film) ν_{max}: 2921, 2852, 1586, 1506, 1492, 1467, 1266, 1236, 749, 693, and 613 cm^{-1}. UV-vis (THF) λ_{max}: 297 nm. Elemental analysis calcd. for $C_{38}H_{55}NO$: C, 84.23; H, 10.23; N, 2.58. Found: C, 84.21; H, 10.27; N, 2.57.

1.3.2 4-Bromo-*N*-(4-bromophenyl)-*N*-(4-((2-octyldodecyl)oxy)phenyl)aniline (2Br-TPAOOD)

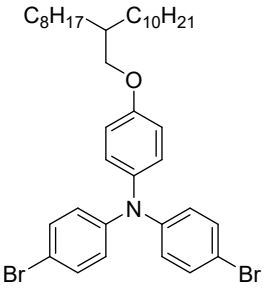

To a round-bottom flask were added TPAOOD (5.4 g, 10 mmol) and THF (40 mL). Subsequently, NBS (4.4 g, 25 mmol) was added to the mixture at 0 °C. After stirring for one hour, the reaction mixture was quenched with a 0.1 M aqueous sodium sulfite solution (30 mL). The resultant mixture was transferred into deionized water (50 mL) and extracted with dichloromethane (3 × 50 mL). The combined organic layers were concentrated under reduced pressure. The residue was purified by column chromatography on silica gel (petroleum ether, 60–90 °C), affording the desired product as a colorless oil (6.9 g, 99% yield). ^{1}H NMR (400 MHz, THF-d_8) δ: 7.21 (d, J = 7.0 Hz, 4H), 6.90 (d, J = 7.0 Hz, 2H), 6.75–6.92 (m, 6H), 3.74 (d, J = 4.2 Hz, 2H), 1.64–1.72 (m, 1H), 1.34–1.12 (m, 32H), and 0.78 (t, J = 5.2 Hz, 6H) ppm. ^{13}C NMR (100 MHz, THF-d_8) δ: 158.05, 148.25, 140.57, 133.12, 128.60, 125.31, 116.55, 115.28, 71.75, 39.32, 33.04, 32.54, 31.17, 30.81, 30.77, 30.73, 30.47, 28.00, 23.72, and 14.60 ppm. HR-MS (ESI) m/z calcd. for $[M]^+$: 699.2468. Found: 699.2485. ATR-FTIR (film) ν_{max}: 2921, 2852, 1506, 1484, 1467, 1312, 1285, 1238, 1072, 1006, 819, and 706 cm^{-1}. UV-vis (THF) λ_{max}: 302 nm. Elemental analysis calcd. for $C_{38}H_{53}Br_2NO$: C, 65.23; H, 7.64; N, 2.00. Found: C, 65.20; H, 7.68; N, 1.99.

1.3.3 4-(2,3-Dihydrothieno[3,4-*b*][1,4]dioxin-5-yl)-*N*-(4-(2,3-dihydrothieno[3,4-*b*][1,4]dioxin-5-yl)phenyl)-*N*-(4-((2-octyldodecyl)oxy)phenyl)aniline (E-TPAOOD-E)

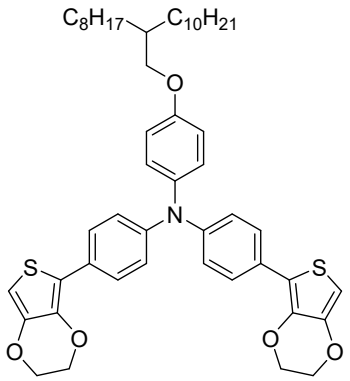

To a round-bottom flask were added 2Br-TPAOOD (3.1 g, 4.5 mmol), 2-(2,3-dihydrothieno[3,4-*b*][1,4]dioxin-5-yl)-4,4,5,5-tetramethyl-1,3,2-dioxaborolane (3.0 g, 11.25 mmol), $Pd(OAc)_2$ (50 mg, 0.225 mmol), SPhos (92 mg, 0.225 mmol), K_3PO_4 (4.8 g, 22.5 mmol), 1,4-dioxane (50 mL), and deionized water (10 mL). The flask was subjected to three cycles of evacuation and argon purging. The reaction mixture was then stirred at 60 °C for 12 hours. After cooling to room temperature, the mixture was filtered through a Kieselguhr pad. The resulting filtrate was concentrated under reduced pressure and purified by column chromatography on silica gel (THF/petroleum ether, 60–90 °C, v/v, 1/5), affording the desired product as a colorless oil (3.2 g, 86% yield). ^{1}H NMR (400 MHz, THF-d_8) δ: 7.43 (d, J = 8.7 Hz, 4H), 6.93 (d, J = 8.9 Hz, 2H), 6.87 (d, J = 8.7 Hz, 4H), 6.76 (d, J = 8.9 Hz, 2H),

6.15 (s, 2H), 4.00–4.11 (m, 4H), 4.12–4.23 (m, 4H), 3.74 (d, J = 5.4 Hz, 2H), 1.63–1.70 (m, 1H), 1.37–1.12 (m, 32H), and 0.78 (t, J = 5.4 Hz, 6H) ppm. ^{13}C NMR (100 MHz, THF-d_8) δ: 157.49, 147.36, 143.72, 128.40, 128.21, 127.54, 123.60, 117.98, 116.28, 97.24, 71.68, 65.87, 65.51, 39.31, 33.04, 32.53, 31.18, 30.81, 30.78, 30.74, 30.48, 28.00, 23.73, and 14.63 ppm. HR-MS *m/z* calcd. for $[M]^+$: 821.4142. Found: 821.4140. ATR-FTIR (film) ν_{max}: 2920, 2851, 1505, 1485, 1435, 1364, 1318, 1236, 1168, 1069, 1027, 923, 901, 825, and 712 cm^{-1}. UV-vis (THF) λ_{max}: 372 nm. Elemental analysis calcd. for $C_{50}H_{63}NO_5S_2$: C, 73.04; H, 7.72; N, 1.70. Found: C, 73.01; H, 7.76; N, 1.67.

1.3.4 p-TPA3Me-E

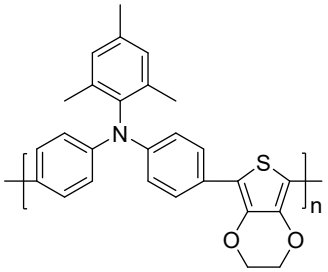

To a dried Schlenk tube were added *N*,*N*-bis(4-bromophenyl)-2,4,6-trimethylaniline (2.2 g, 5.0 mmol), 3,4-ethylenedioxythiophene (711 mg, 5.0 mmol), $Pd(OAc)_2$ (225 mg, 1.0 mmol), $HP(Cy)_3BF_4$ (737 mg, 2.0 mmol), K_2CO_3 (2.1 g, 15.0 mmol), and DMAc (200 mL). The tube was evacuated and purged with argon three times. The reaction mixture was stirred at 130 °C under an argon atmosphere for 1 hour. After cooling to room temperature, the solvent was removed using a rotary evaporator. The residue was purified by column chromatography on silica gel using toluene/petroleum ether (*v*/*v*, 1/1) and toluene as eluents. The toluene fraction was collected, concentrated to a small volume, and added dropwise to methanol (200 mL). After filtration and drying, the desired product was obtained as a green-yellow powder (1.4 g, 68% yield). ^{1}H NMR (400 MHz, THF-d_8) δ: 7.46 (d, J = 8.5 Hz, 4H), 6.88–6.79 (m, 6H), 4.18–4.40 (m, 4H), 2.19 (s, 3H), and 1.88 (d, J = 9.6 Hz, 6H) ppm. ^{13}C NMR (100 MHz, THF-d_8) δ: 143.56, 139.27, 137.70, 136.88, 129.52, 129.42, 126.06, 125.76, 118.89, 113.46, 64.16, 19.76, and 17.38 ppm. ATR-FTIR (film) ν_{max}: 2919, 2854, 1586, 1499, 1438, 1317, 1237, 1086, 915, 824, and 719 cm^{-1}. UV-vis (THF) λ_{max}: 427 nm. Elemental analysis calcd. for $(C_{27}H_{23}NO_2S)_n$: C, 76.21; H, 5.45; N, 3.29. Found: C, 76.17; H, 5.48; N, 3.25.

1.3.5 p-TPA3Me-E-TPAOOD-E

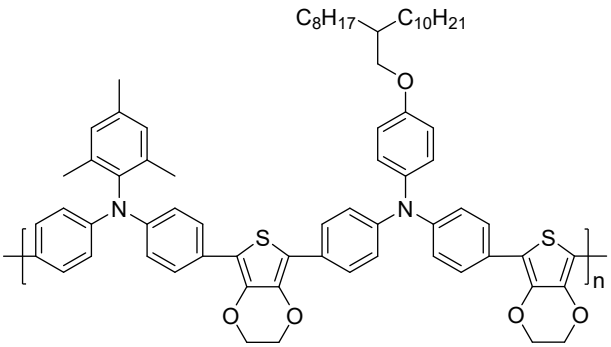

To a dried Schlenk tube were added *N*,*N*-bis(4-bromophenyl)-2,4,6-trimethylaniline (1.11 g, 2.5 mmol), E-

TPAOOD-E (2.02 g, 2.5 mmol), $Pd(OAc)_2$ (112 mg, 0.5 mmol), $HP(Cy)_3BF_4$ (368 mg, 1.0 mmol), K_2CO_3 (1.0 g, 7.5 mmol), and DMAc (100 mL). The tube was evacuated and purged with argon three times. The reaction mixture was stirred at 130 °C under an argon atmosphere for 1 hour. After cooling to room temperature, the solvent was removed using a rotary evaporator. The residue was purified by column chromatography on silica gel using toluene/petroleum ether (*v*/*v*, 1/1) and toluene as eluents. The toluene fraction was collected, concentrated to a small volume, and added dropwise to methanol (200 mL). After filtration and drying, the desired product was obtained as a light green powder (2.1 g, 76% yield). ^{1}H NMR (400 MHz, THF-d_8) δ: 7.77–7.13 (m, 8H), 6.98–6.73 (m, 14H), 4.26–4.06 (m, 8H), 3.75 (d, J = 6.0 Hz, 2H), 2.19 (br, J = 4.5 Hz, 3H), 2.03–1.76 (m, 6H), 1.64–1.73 (m, 1H), 1.40–1.16 (m, 32H), and 0.77 (t, J = 5.7 Hz, 6H) ppm. ^{13}C NMR (100 MHz, THF-d_8) δ: 157.52, 147.23, 145.18, 141.15, 140.84, 139.43, 139.24, 138.44, 130.96, 128.22, 127.63, 127.53, 127.28, 123.65, 120.46, 116.30, 115.32, 114.87, 71.72, 65.71, 39.34, 33.05, 32.56, 31.19, 30.78, 30.49, 28.01, 23.74, 21.30, 18.92, and 14.63.ppm. ATR-FTIR (film) ν_{max}: 2921, 2849, 1594, 1499, 1436, 1318, 1237, 1084, 914, 825, and 720 cm^{-1}. UV-vis (THF) λ_{max}: 430 nm. Elemental analysis calcd. for $(C_{71}H_{80}N_2O_5S_2)_n$: C, 77.14; H, 7.29; N, 2.53. Found: C, 77.11; H, 7.35; N, 2.50.

1.3.6 p-TPAOOD-E

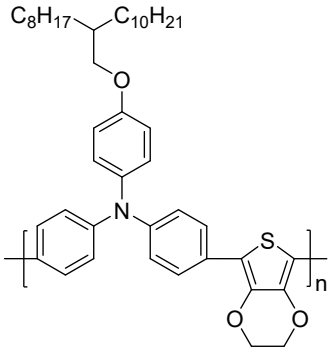

To a dried Schlenk tube were added 2Br-TPAOOD (1.7 g, 2.5 mmol), 3,4-ethylenedioxythiophene (356 mg, 2.5 mmol), $Pd(OAc)_2$ (112 mg, 0.5 mmol), $HP(Cy)_3BF_4$ (368 mg, 1.0 mmol), K_2CO_3 (1.0 g, 7.5 mmol), and DMAc (100 mL). The tube was evacuated and purged with argon three times. The reaction mixture was stirred at 130 °C under an argon atmosphere for 1 hour. After cooling to room temperature, the solvent was removed using a rotary evaporator. The residue was purified by column chromatography on silica gel using toluene/petroleum ether (*v*/*v*, 1/1) and toluene as eluents. The toluene fraction was collected, concentrated to a small volume, and added dropwise to methanol (200 mL). After filtration and drying, the desired product was obtained as a light green powder (1.2 g, 72% yield). ^{1}H NMR (400 MHz, THF-d_8) δ: 7.55–7.43 (m, 4H), 6.99–6.86 (m, 6H), 6.80–6.73 (m, 2H), 4.13–4.26 (m, 4H), 3.78–3.70 (m, 2H), 1.63–1.71 (m, 1H), 1.35–1.11 (m, 32H), and 0.81–0.74 (m, 6H) ppm. ^{13}C NMR (100 MHz, THF-d_8) δ: 157.55, 147.27, 141.13, 139.44, 128.26, 128.21, 127.56, 123.66, 116.32, 115.16, 71.73, 65.73, 39.34, 33.05, 32.56, 31.19, 30.82, 30.78, 30.74, 30.48, 28.02, 23.74, and 14.63 ppm. ATR-FTIR (film) ν_{max}: 2921, 2852, 1500, 1437, 1360, 1319, 1237, 1086, 1034, 915, 827, and 725 cm^{-1}. UV-vis (THF) λ_{max}: 434 nm. Elemental analysis calcd. for $(C_{44}H_{57}NO_3S)_n$: C, 77.72; H, 8.45; N, 2.06. Found: C, 77.68; H, 8.49; N, 2.07.

1.4 Cyclic voltammetry measurements

Cyclic voltammograms were recorded using a CHI660E electrochemical workstation (CH Instruments). A 10 μL solution of the polymeric semiconductor in chlorobenzene (5 mg mL^{-1}) was drop-cast onto the pre-cleaned surface of a 3 mm diameter glassy carbon electrode and air-dried, forming a modified working electrode. The electrolytic cell comprised the modified working electrode, a fluorine-doped tin oxide counter electrode, and an Ag/AgCl (sat. KCl) reference electrode. EMITFSI (0.1 M in MeCN) was employed as the supporting electrolyte. The scan rate was maintained at 50 mV s^{-1}. All potentials are referenced against ferrocene.

1.5 Ultraviolet photoelectron spectroscopy (UPS) measurements

Indium-doped tin oxide (ITO) glass substrates (12 Ω sq^{-1}, 1.6 mm thickness) were sequentially sonicated in detergent, deionized water, acetone, and ethanol for 15 minutes each. Subsequently, the substrates underwent UV-ozone treatment for 15 minutes to activate the surface. A uniform layer of PEDOT:PSS was then spin-coated at 3000 rpm for 30 seconds onto the prepared ITO substrate and annealed at 150 °C for 30 minutes. After cooling to room temperature, a polymeric semiconductor layer was deposited via spin-coating at 3000 rpm for 30 seconds using a chlorobenzene solution containing either p-TPA3Me-E, p-TPA3Me-E-TPAOOD-E, or p-TPAOOD-E at a concentration of 50 mg mL^{-1}. UPS spectra were recorded using an ESCALAB XI+ instrument (Thermo Fisher).

1.6 Hole densities in pristine organic semiconductor films

To quantify the hole density (p) of pristine polymeric semiconductors, impedance spectroscopy measurements were performed on metal-insulator-semiconductor (MIS) devices. The MIS device architecture consisted of layers of n^{++}-Si/SiO_2/p-BCB/polymeric semiconductor/Au. The p-BCB layer was formed by spin-coating a BCB chlorobenzene solution (1 mg mL^{-1}) at 4000 rpm for 30 seconds, followed by annealing at 250 °C for 1 hour. Subsequently, a polymeric semiconductor layer was spin-coated from a chlorobenzene solution containing 132 mM TBP and p-TPA3Me-E (50 mg mL^{-1}), p-TPA3Me-E-TPAOOD-E (50 mg mL^{-1}), or p-TPAOOD-E (50 mg mL^{-1}) at 1500 rpm for 30 seconds, followed by the thermal evaporation of gold contacts (approximately 100 nm). Impedance spectra were acquired using an Autolab PGSTAT302N electrochemical workstation (Metrohm) over a frequency range of 10 Hz to 3 MHz with a perturbation of 20 mV. The capacitance (C) was calculated using the equation: $C = -\frac{1}{\omega}\left[\frac{Z'' - \omega L_i}{(Z' - R_s)^2 + (Z'' - \omega L_i)^2}\right]$, where ω is the angular frequency, Z' and Z'' are the real and imaginary components of impedance, R_s is the series resistance, and L_i is the parasitic inductance. The p was extracted from the slope of the Mott-Schottky plot using the equation: $p = \frac{2}{q\varepsilon_r\varepsilon_0 \frac{d(A/C)^2}{dV}}$, where q is the elementary charge, ε_r is the relative permittivity, ε_0 is the vacuum permittivity, and A is the area of the MIS device.

1.7 Hole extraction

The glass slides were sequentially sonicated in detergent, deionized water, acetone, and ethanol for 15 minutes each. Following this cleaning process, the slides were treated with UV-ozone for 15 minutes and then transferred into a glove box filled with dry air (relative humidity < 3%). The fabrication of the $FAPbI_3$ perovskite layer involved a two-step spin-coating process. Initially, a solution containing 1.5 M PbI_2 and 7.5 mM RbCl in a DMF:DMSO solvent mixture (9:1 volume ratio) was spin-coated onto the cleaned glass slides at 1500 rpm for 30 seconds, followed by annealing at 70 °C for 1 minute. Subsequently, a solution mixture of FAI:MACl (90 mg:13.5 mg in 1 mL IPA) was spin-coated onto the PbI_2 layer at 1800 rpm for 30 seconds. The resulting film was annealed at 150 °C for 30 minutes, forming the $FAPbI_3$ perovskite layer with a minor quantity of $(PbI_2)_2RbCl$.[5] For the passivation layer, a TTI-derived interlayer (2.5 mg mL^{-1} in chlorobenzene) was spin-coated at 5000 rpm for 30 seconds and annealed at 85 °C for 20 minutes.[4] Subsequently, a chlorobenzene solution containing polystyrene (50 mg mL^{-1}), spiro-OMeTAD (50 mg mL^{-1}), PTAA (50 mg mL^{-1}), p-TPA3Me-E (50 mg mL^{-1}), p-TPA3Me-E-TPAOOD-E (50 mg mL^{-1}), or p-TPAOOD-E (50 mg mL^{-1}) was spin-coated at 5000 rpm for 30 seconds. Steady-state and time-resolved photoluminescence decay measurements were performed using a Life-Spec-II fluorescence spectrometer (Edinburgh Instruments). Photoluminescence mapping was performed employing a laser confocal fluorescence lifetime/intensity imaging system (MicroTime200, PicoQuant) equipped with a 640 nm picosecond pulsed diode laser for excitation.

1.8 Direct-current conductivity measurements

The direct-current conductivities (σ) of both pristine and composite organic semiconductor films were determined by obtaining current–voltage (I–V) curves across potential biases ranging from −1.0 V to 1.0 V. The films were deposited onto interdigital gold electrodes comprising 119 channels, each with a channel length (L) of 1.5 mm, a channel width (W) of 10 μm, and a channel thickness (t) of 110 nm. An organic semiconductor layer was spin-coated from a chlorobenzene solution containing spiro-OMeTAD (50 mg mL^{-1}), PTAA (50 mg mL^{-1}), p-TPA3Me-E (50 mg mL^{-1}), p-TPA3Me-E-TPAOOD-E (50 mg mL^{-1}), or p-TPAOOD-E (50 mg mL^{-1}), each in combination with 132 mM TBP and varying weight percentages of TBPH-HFSI (0%, 5%, 10%, or 15%), at 1500 rpm for 30 seconds. Prior to measurement, the devices were stored in a dry air environment (< 5% relative humidity) for 7 days. I–V measurements were conducted using a Keithley 2400 source meter, with test automation facilitated by Labview 14.0. The calculation of σ was performed using the formula $\sigma = sW/nLt$, where s represents the slope obtained from linear fitting of the I–V plot.

1.9 Hole densities in organic semiconductor composite films

The determination of p for an organic semiconductor film containing TBPH-HFSI presented a challenge. To address this, we adopted a comparative approach based on the quadratic integral intensities of electron paramagnetic resonance (EPR) signals from organic semiconductor films with and without TBPH-HFSI. The established p value for a pristine organic semiconductor film served as the reference. For EPR spectrum acquisition, a chlorobenzene solution was applied to a 2 cm × 2 cm microslide using the drop-casting method. The microslide was then crushed and transferred into a borosilicate glass tube. The chlorobenzene solutions contained spiro-

OMeTAD (50 mg mL^{-1}), PTAA (50 mg mL^{-1}), p-TPA3Me-E (50 mg mL^{-1}), p-TPA3Me-E-TPAOOD-E (50 mg mL^{-1}), or p-TPAOOD-E (50 mg mL^{-1}), each combined with 132 mM TBP and varying weight percentages of TBPH-HFSI (0%, 5%, 10%, or 15%). EPR measurements were conducted using a Bruker EMXplus EPR spectrometer.

1.10 Perovskite solar cells

1.10.1 Fabrication

The cleaned ITO substrates were treated with UV-ozone for 15 minutes prior to use. A diluted SnO_2 colloid dispersion was filtered through a 0.2 μm PTFE filter. This refined solution was then spin-coated onto the pristine ITO substrate at 4000 rpm for 30 seconds, followed by annealing at 150 °C for 30 minutes in ambient air.[6] Following UV-ozone treatment, the glass/ITO/SnO_2 substrates were transferred into a glove box with dry air (< 3% relative humidity) for the deposition of the perovskite layer, TTI-derived interlayer, and hole transport layers, as detailed in Section 1.7. Finally, a gold electrode (~100 nm) was deposited using a shadow mask under a vacuum of $\leq 1 \times 10^{-4}$ Pa. The resulting device, with an active area of 0.10 cm^2, was laminated with a high-quality anti-reflective film on the glass side. The cell was then covered with waterproof adhesive tape on the gold electrode side, sealed with epoxy adhesive (3M), and stored in dry air overnight.

1.10.2 Optoelectronic measurements

The current density–voltage characteristics were measured using a Keithley 2400 source meter, with test automation facilitated by LabVIEW 14.0. Illumination was provided by an LS1000-4S-AM solar simulator (Solar Light Company), delivering AM1.5G irradiation at 100 mW cm^{-2}, with intensity validated against a calibrated silicon solar cell. A black metal mask with an aperture area of 0.07 cm^2 was employed to precisely define the photoactive region. Device examination was performed through both reverse and forward scans at a scan rate of 50 mV s^{-1}. For external quantum efficiency (EQE) measurements, an Omni-λ300 monochromator (Zolix) and a 150 W xenon lamp (Zolix) were used, with photocurrent data recorded by a Keithley 2400 source meter. Monochromatic light intensity was quantified using a Hamamatsu S1337-1010BQ silicon diode calibrated by the National Institute of Metrology, China. Light emitting diode operation measurements were conducted within a nitrogen-filled glovebox at room temperature. For the assessment of electroluminescence external quantum efficiency (EQE_{EL}), a custom setup featuring a 2400 source meter (Keithley), an FOIS-1 integration sphere (Ocean Insight), and a QE Pro spectrometer (Ocean Insight) was utilized.

1.10.3 Storage stability at 85 °C

To evaluate the dark storage stability at 85 °C (ISOS-D-2), perovskite solar cells were placed on a hot plate in dry air. Periodic *J–V* measurements were conducted under AM1.5G conditions to monitor performance parameters.

1.10.4 Humidity stability

To evaluate the humidity stability at ambient temperature, encapsulated perovskite solar cells were placed within a sealed buckle box filled with water at the bottom, ensuring an internal humidity approximating 100%. Periodic evaluation of the cell performance was carried out through *J–V* measurement under simulated AM1.5G sunlight.

1.10.5 Operational stability at 45 °C

Maximum power point (MPP) tracking was performed using a 16-channel photovoltaic tracking system from YH Electronic Equipment Business, in conjunction with the SLS-LED-80A solar simulator by Qingdao Solar Scientific Instrument High-tech Co., LTD. The experiment was conducted in a nitrogen-filled glovebox to maintain controlled conditions. MPP data were collected at 5-minute intervals using the perturb and observe method.

1.10.6 Device dismantling

The dismantling process began with the meticulous removal of the epoxy adhesive and waterproof adhesive tape, leading to the partial detachment of the gold electrode. Subsequently, a layer of magic tape (Scotch, 3M) was applied to the remaining gold layer. Upon careful removal of the magic tape, the gold layer was eliminated. If necessary, the hole transport layers were further cleaned through five cycles of dynamic spin-coating with chlorobenzene.

2 Theoretical modeling

2.1 Density functional theory calculation

The frontier molecular orbitals were calculated using the Gaussian 16 program suite within the framework of periodic boundary condition-density functional theory or density functional theory at the B3LYP/6-311G(d,p) level. Visualization of the frontier molecular orbitals was accomplished with GaussView 5.0.

2.2 Molecular dynamics simulation

Polymer chains with a molecular weight of approximately 10 kDa were constructed using the Build Polymer tool in Materials Studio 8.0. Cubic boxes with periodic boundaries were then generated using the Amorphous Cell module, accommodating 10 polymer chains. Molecular dynamics simulations were performed with the COMPASS II force field. Glass transition temperature and diffusivity studies were carried out using the FORCITE module in Materials Studio 8.0. The simulation protocol began with an initial NVT simulation at 700 K using a Nose thermostat, followed by an NPT simulation at 700 K utilizing both a Nose thermostat and a Berendsen barostat. A stepwise cooling process from 700 K to 200 K was then executed, with NVT and NPT simulations conducted at each temperature. Specific volumes were recorded after full equilibration at each temperature. The theoretical glass transition temperature was determined by intersecting the linear fitting lines in the low and high-temperature regimes. Composites of organic semiconductor and salt were modeled with TBPH-HFSI molecules at a weight

percentage of 15%. Additionally, FAI was introduced into the composites, and further NVT and NPT simulations were conducted. The mean square displacements of the recorded trajectories were analyzed to determine theoretical diffusivities.

3 Supplementary figures and tables

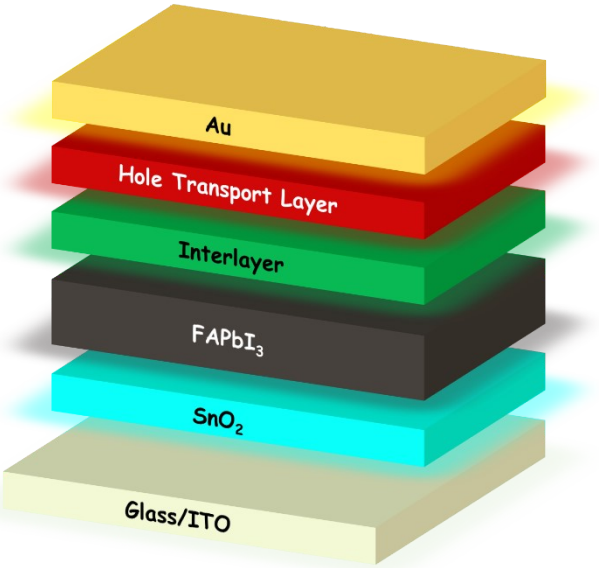

Fig. S1 Schematic illustration of a multilayered n-i-p perovskite solar cell. ITO denotes indium tin oxide, SnO_2 serves as the electron transport layer, $FAPbI_3$ constitutes the light-absorbing layer, and Au symbolizes the gold electrode. For enhanced efficiency, an interlayer is incorporated to passivate the $FAPbI_3$ layer.

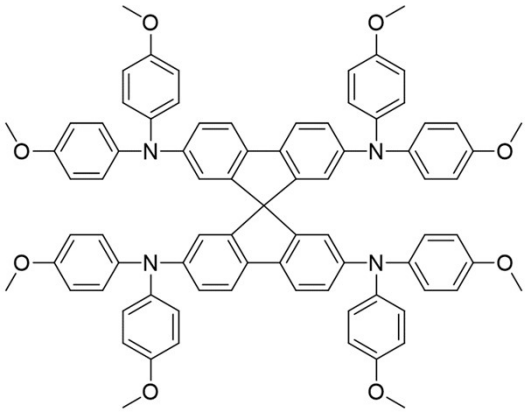

Fig. S2 Chemical structure of spiro-OMeTAD.

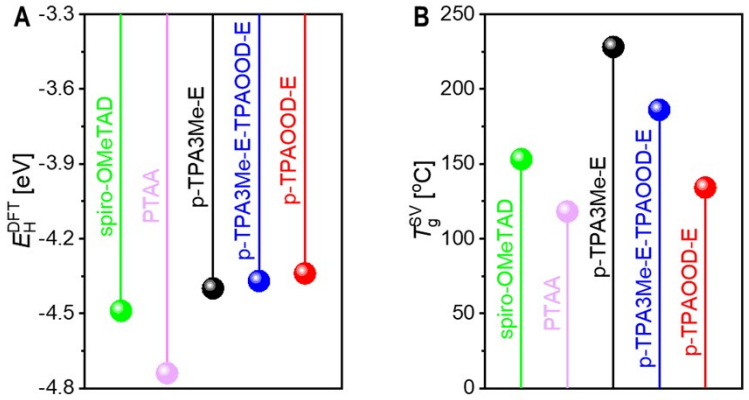

Fig. S3 (A) Highest occupied molecular orbital (HOMO) energy levels ($E_{\mathrm{H}}^{\mathrm{DFT}}$) obtained from density functional theory calculations, with ethoxy substitution for 2-octyldodecyloxy to enhance computational efficiency. (B) Glass transition temperatures ($T_{\mathrm{g}}^{\mathrm{SV}}$) derived from molecular dynamics simulations of temperature-dependent specific volumes.

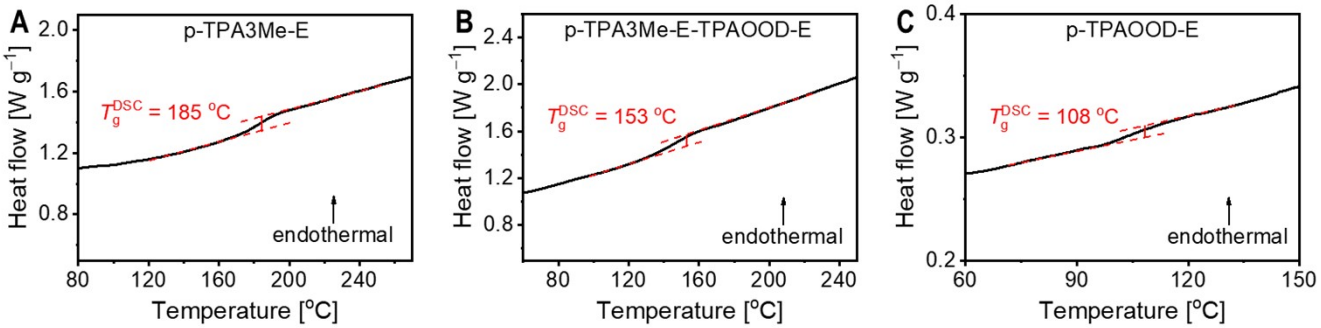

Fig. S4 Differential scanning calorimetry curves, with the glass transition temperature ($T_{\mathrm{g}}^{\mathrm{DSC}}$) indicated.

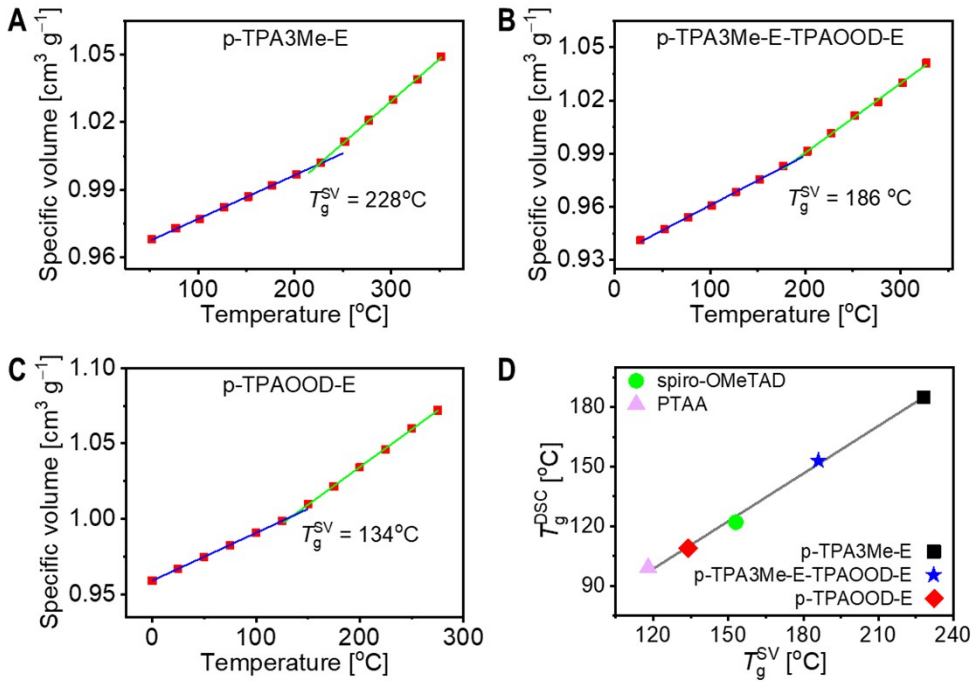

Fig. S5 (A–C) Specific volume as a function of temperature from molecular dynamics simulations. The blue and green solid lines represent linear fits for the low-temperature and high-temperature regions, respectively. The intersection of these lines corresponds to the theoretical glass transition temperature ($T_{\mathrm{g}}^{\mathrm{SV}}$). (D) Correlation between the glass transition temperature determined by differential scanning calorimetry ($T_{\mathrm{g}}^{\mathrm{DSC}}$) and $T_{\mathrm{g}}^{\mathrm{SV}}$. Data for spiro-

OMeTAD and PTAA are also included for comparison.[7]

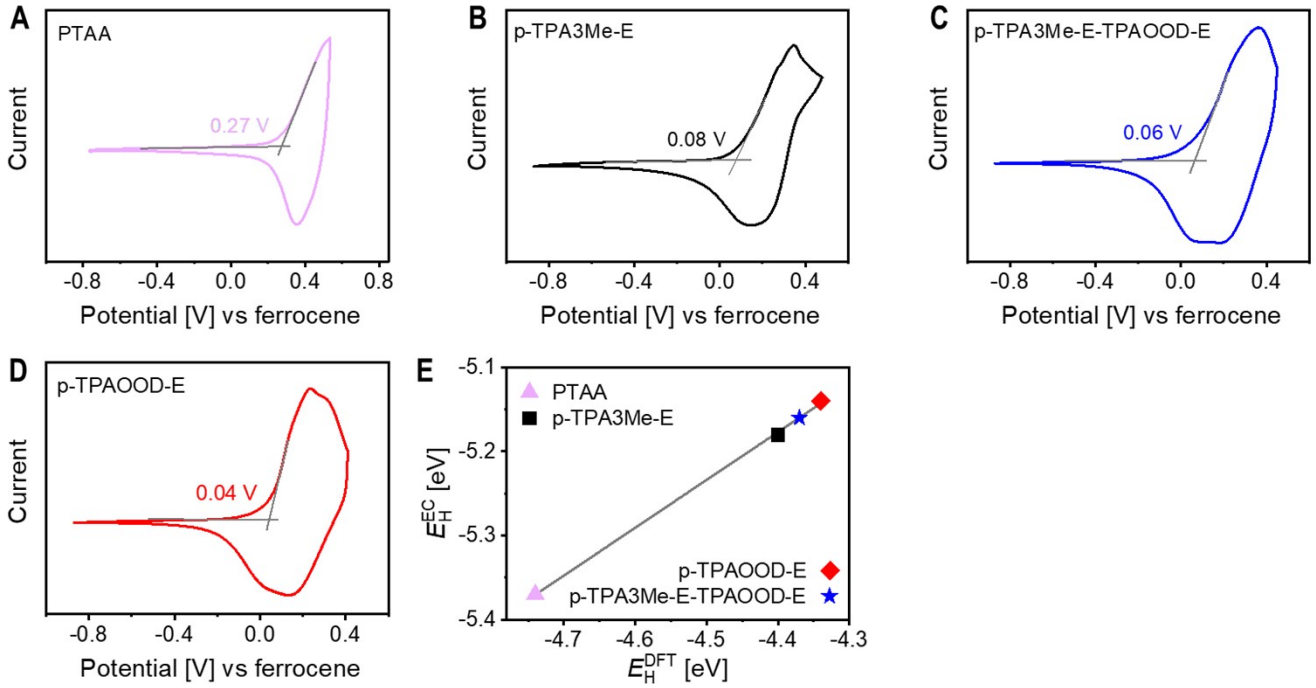

Fig. S6 (A–D) Thin-film cyclic voltammograms of four triphenylamine-based polymers. The intersection of the tangent to the oxidation wave and the baseline parallel to the *x*-axis defines the oxidation onset potential (V_{onset}), which is indicated for each polymer. The HOMO energy levels (E_H^{EC}) were calculated using the equation $E_H^{EC} = -5.10 - V_{onset}$.[8] The E_H^{EC} value for PTAA, p-TPA3Me-E, p-TPA3Me-E-TPAOOD-E, and p-TPAOOD-E is −5.27 eV, −5.18 eV, −5.16 eV, and −5.12 eV, respectively. It should be noted that due to the relatively high solubility of spiro-OMeTAD in acetonitrile, a reliable thin-film cyclic voltammogram could not be obtained using this method. (E) Correlation between E_H^{EC} and the HOMO energy levels calculated by density functional theory (E_H^{DFT}).

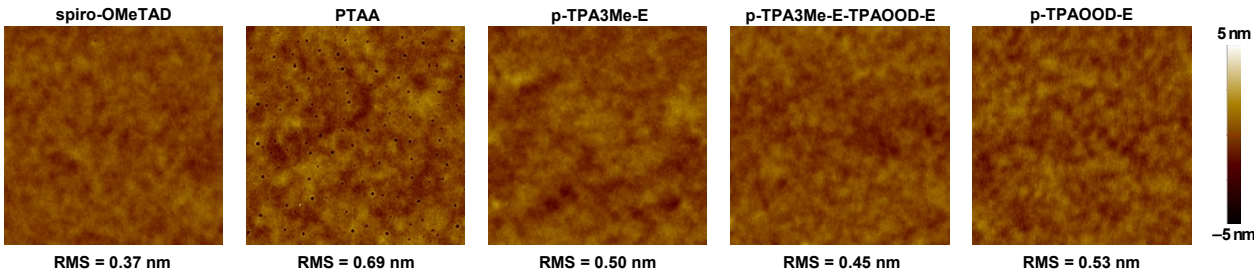

Fig. S7 Atomic force microscopy images of pristine organic semiconductor films spin-coated on PEDOT:PSS substrates. The root mean square (RMS) roughness values are shown below each image. Image size: 5 μm × 5 μm.

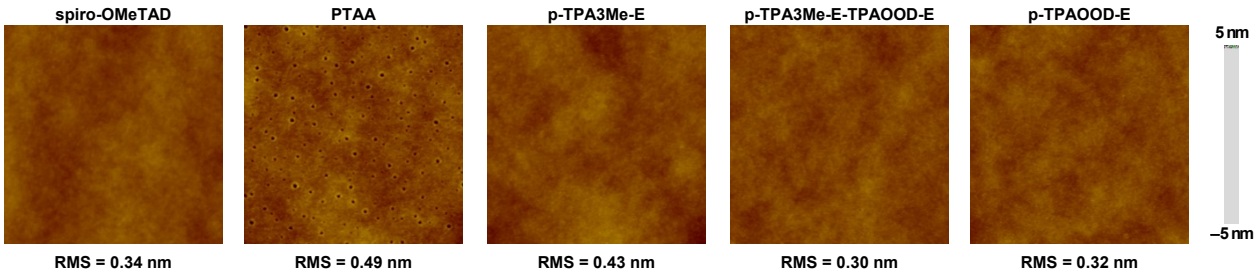

Fig. S8 Atomic force microscopy images of pristine organic semiconductor films spin-coated on monocrystalline silicon substrates. The root mean square (RMS) roughness values are shown below each image. Image size: 5 μm × 5 μm.

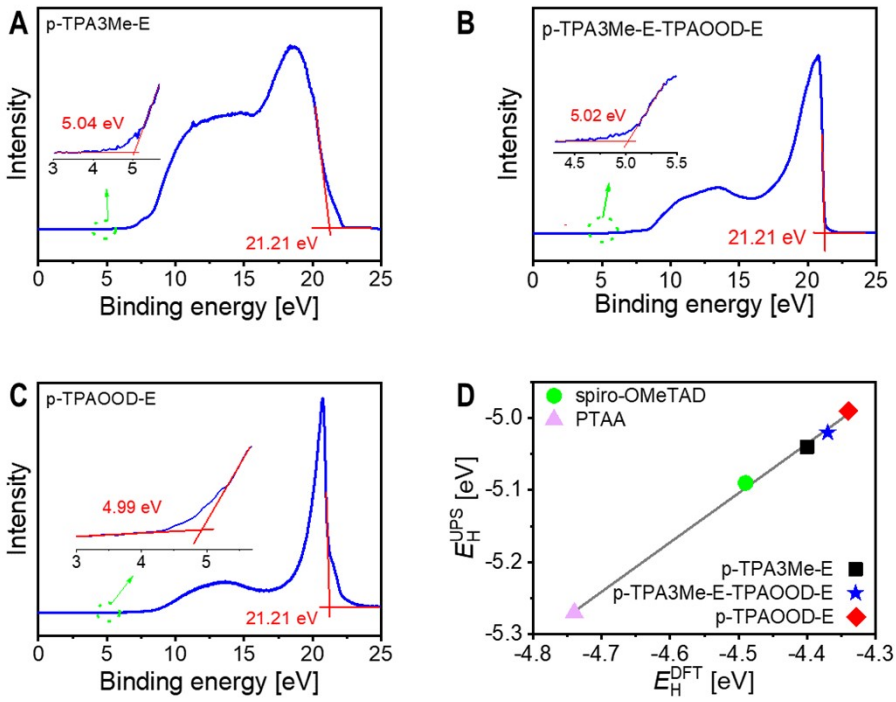

Fig. S9 (A–C) Ultraviolet photoelectron spectra of polymeric semiconductors spin-coated on ITO/PEDOT:PSS substrates. The spectra are calibrated using the cutoff energy corresponding to He I photon energy (21.21 eV). The inset shows an enlarged view of the onset region. The intersection of the tangent to the spectrum in the low binding energy region with the baseline parallel to the *x*-axis defines the HOMO energy level ($E_{\mathrm{H}}^{\mathrm{UPS}}$). (D) Correlation between $E_{\mathrm{H}}^{\mathrm{UPS}}$ and theoretically calculated HOMO energy level ($E_{\mathrm{H}}^{\mathrm{DFT}}$). Data for spiro-OMeTAD and PTAA are also included for comparison.[7]

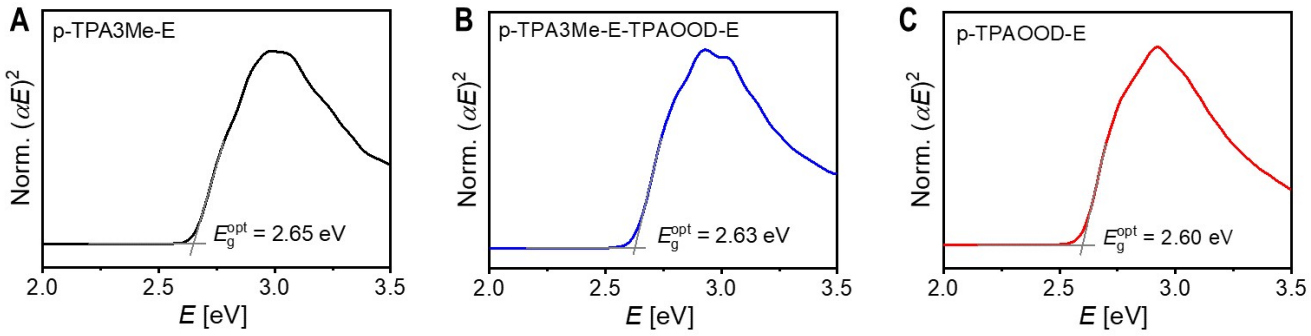

Fig. S10 Tauc plots of polymeric semiconductors spin-coated on quartz substrates. Here, E, α, and E_g^{opt} denote photon energy, optical absorption coefficient, and optical bandgap, respectively. The intersection of the tangent to the curve in the low-energy region with the baseline parallel to the x-axis determines E_g^{opt}.

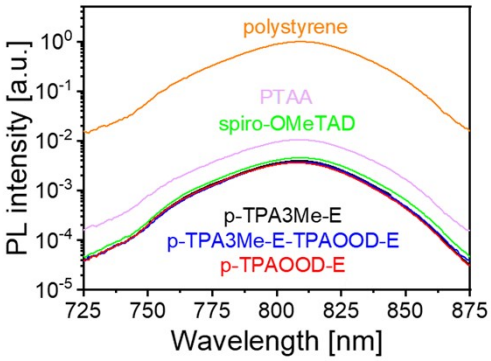

Fig. S11 Steady-state photoluminescence spectra of perovskite films on glass substrate covered with polystyrene and various organic semiconductors.

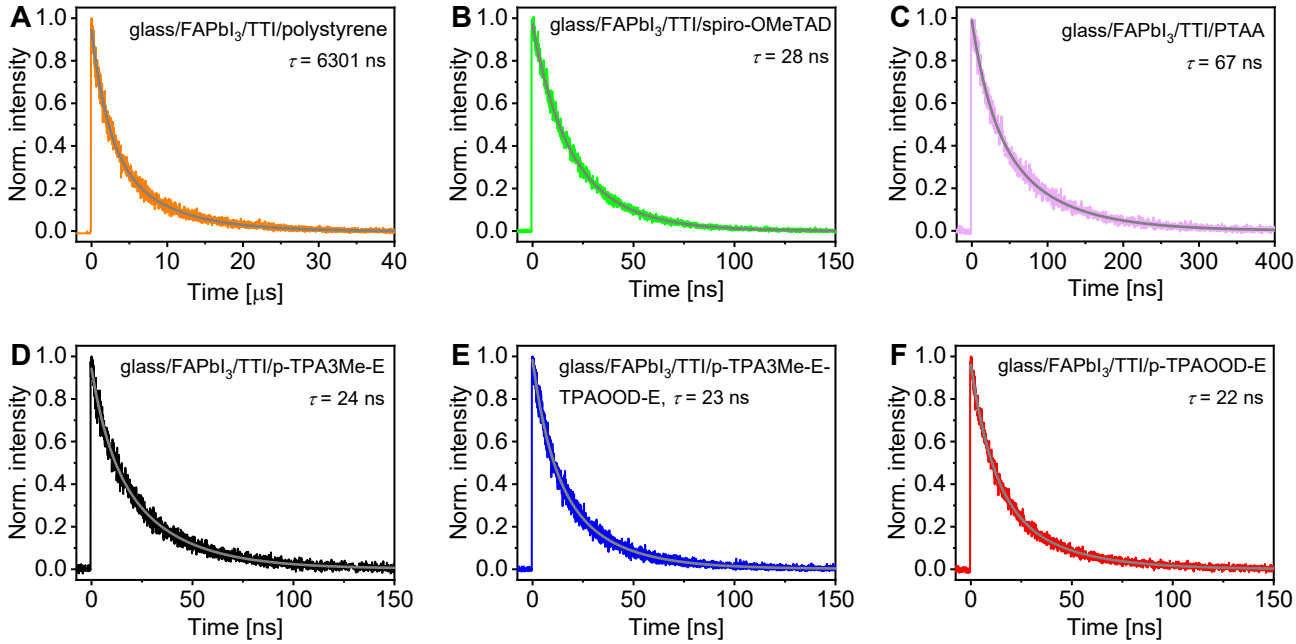

Fig. S12 (A–F) Time-resolved photoluminescence traces at 810 nm of TTI-modified $FAPbI_3$ films on glass substrates. The perovskite layer is overlaid with a thin film of polystyrene or p-type organic semiconductor. The gray curve represents a double-exponential decay fit, providing fitting parameters used to calculate the amplitude-weighted photoluminescence lifetime (τ). Excitation wavelength: 670 nm.

Table S1. Fit parameters of photoluminescence decays for $FAPbI_3$ films coated with various organic layers on glass substrates, encompassing the amplitude-weighted photoluminescence lifetime, hole extraction rate constant, and hole extraction yield[a]

Sample	τ_1 [ns]	A_1	τ_2 [ns]	A_2	τ [ns]	k_{he} [μs^{-1}]	ϕ_{he} [%]
glass/$FAPbI_3$/TTI/polystyrene	3051.1	0.56	10437.2	0.44	6301.0	/	/
glass/$FAPbI_3$/TTI/spiro-OMeTAD	16.9	0.34	33.9	0.66	28.1	35.6	99.6
glass/$FAPbI_3$/TTI/PTAA	31.0	0.44	95.7	0.56	67.2	14.9	98.9
glass/$FAPbI_3$/TTI/p-TPA3Me-E	9.2	0.34	31.5	0.66	23.9	41.7	99.6
glass/$FAPbI_3$/TTI/p-TPA3Me-E-TPAOOD-E	11.3	0.46	32.6	0.54	22.8	43.7	99.6
glass/$FAPbI_3$/TTI/p-TPAOOD-E	35.2	0.43	12.3	0.57	22.1	45.1	99.6

[a] τ_1 and τ_2 represent the time constants of photoluminescence decay, A_1 and A_2 represent the relative amplitudes, and τ represents the amplitude-weighted average photoluminescence lifetime obtained by using equation $\tau = A_1\tau_1 + A_2\tau_2$. The hole extraction rate constant (k_{he}) is obtained by using equation $k_{he} = (\tau_{PS} - \tau_{OSC}) / (\tau_{PS} \times \tau_{OSC})$. ϕ_{he} represents the hole extraction yield obtained by using equation $\phi_{he} = (\tau_{PS} - \tau_{OSC}) / \tau_{PS}$ where τ_{PS} represents amplitude-weighted average photoluminescence lifetime of the glass-supported $FAPbI_3$ film covered with polystyrene (PS), and τ_{OSC} represents the amplitude-weighted average photoluminescence lifetime of the glass-supported $FAPbI_3$ film covered with p-type organic semiconductors (OSC).

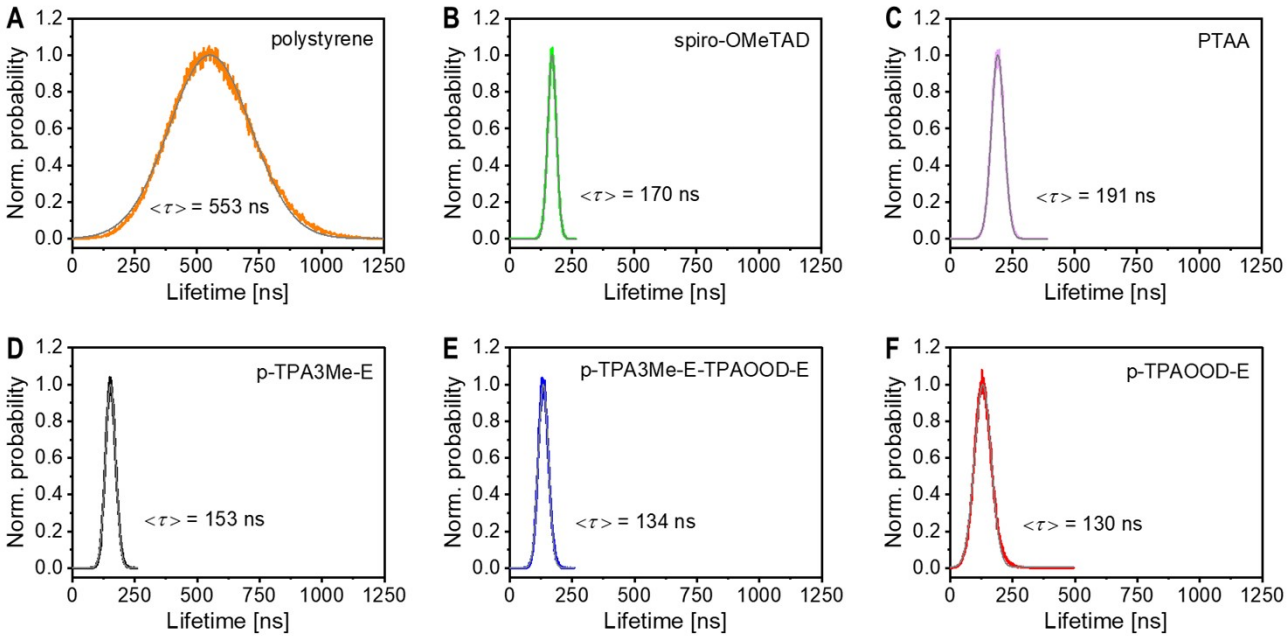

Fig. S13 (A–F) Statistical distributions of photoluminescence lifetime for perovskite films on glass substrate covered with polystyrene and various organic semiconductors. Excitation wavelength: 640 nm. The average photoluminescence lifetimes ($<\tau>$) obtained by Gaussian fitting are also provided.

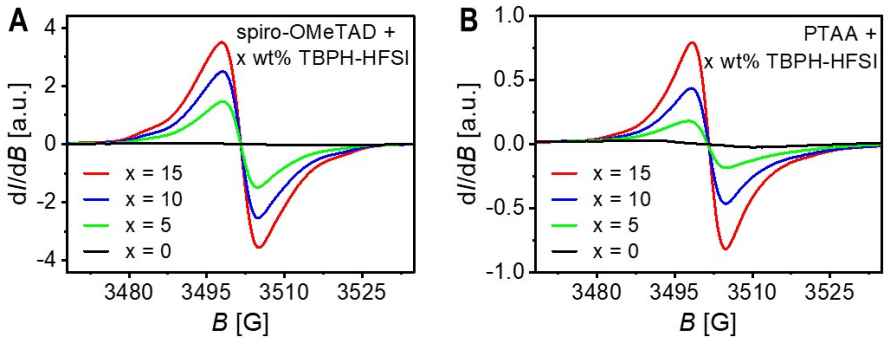

Fig. S14 Electron paramagnetic resonance (EPR) spectra of spiro-OMeTAD (A) and PTAA (B) films containing varying weight percentages (x wt%) of TBPH-HFSI. d*I*/d*B* represents the first derivative of absorption intensity (*I*), with *B* denoting the magnetic field strength.

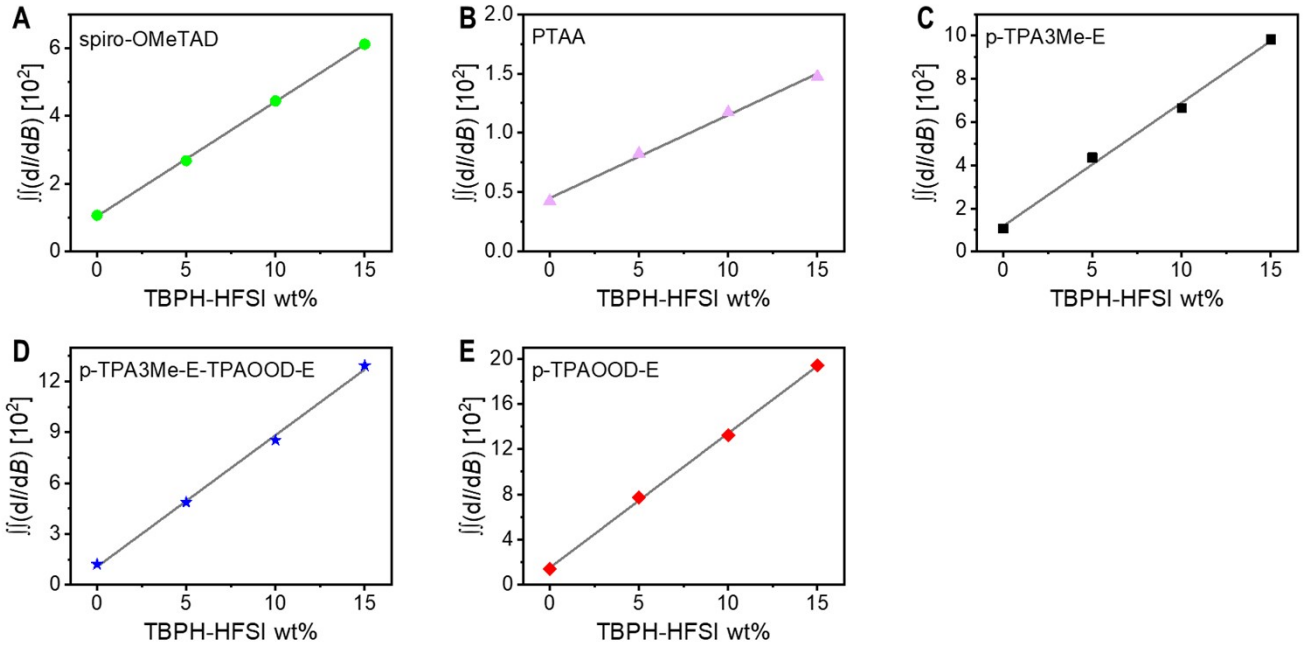

Fig. S15 Relationships between the quadratic integral of EPR signal (∬(d*I*/d*B*)) and the weight percentage (wt%) of TBPH-HFSI. The solid lines depict linear fits.

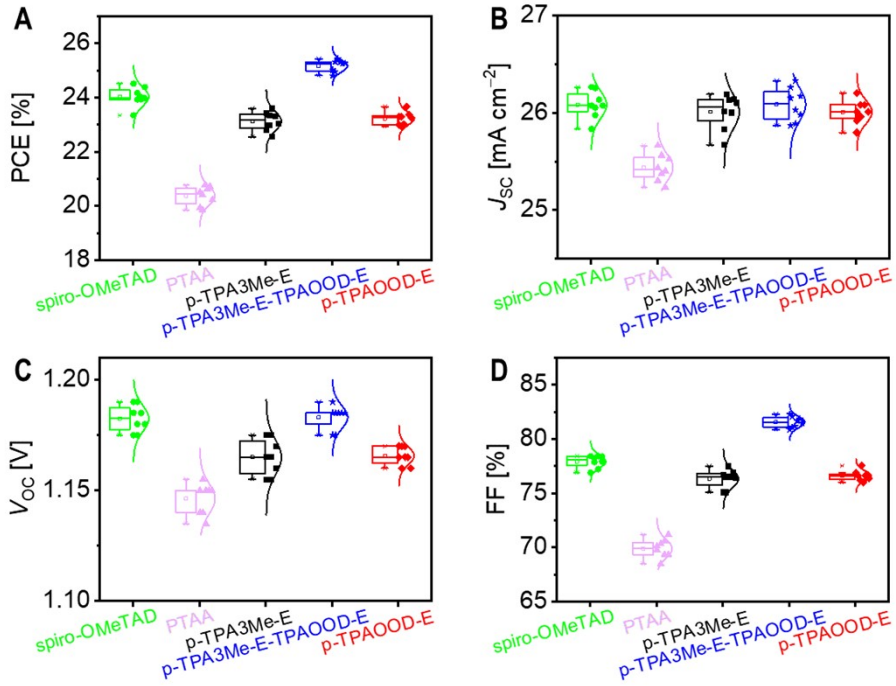

Fig. S16 (A–D) Photovoltaic parameter statistics for as-prepared perovskite solar cells employing various hole transport layers containing 15 wt% TBPH-HFSI, under AM1.5G simulated sunlight irradiation (100 mW cm^{-2}): (A) power conversion efficiency (PCE); (B) short-circuit current density (J_{SC}); (C) open-circuit voltage (V_{OC}); (D) fill factor (FF).

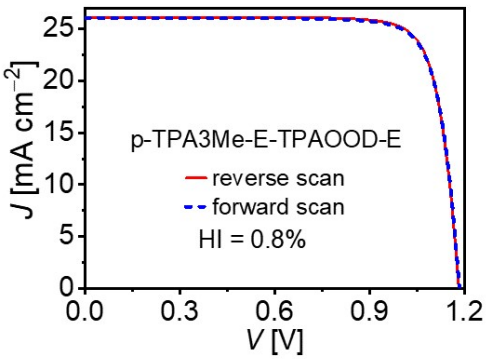

Fig. S17 Forward and reverse photocurrent density–voltage (J–V) scan of the representative p-TPA3Me-E-TPAOOD-E cell under AM1.5G illumination at 100 mW cm^{-2}. The hysteresis index (HI) is calculated as ($PCE_{reverse}$ – $PCE_{forward}$) / $PCE_{reverse}$.

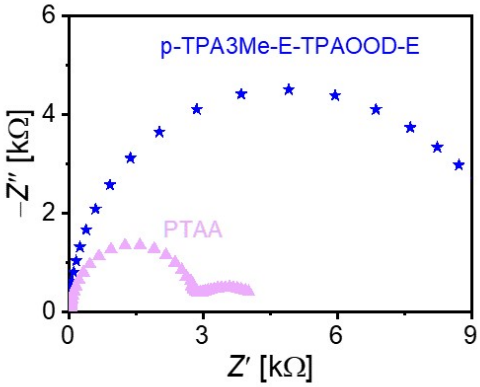

Fig. S18 Electrical impedance spectra of cells employing p-TPA3Me-E-TPAOOD-E and PTAA as hole transport materials.

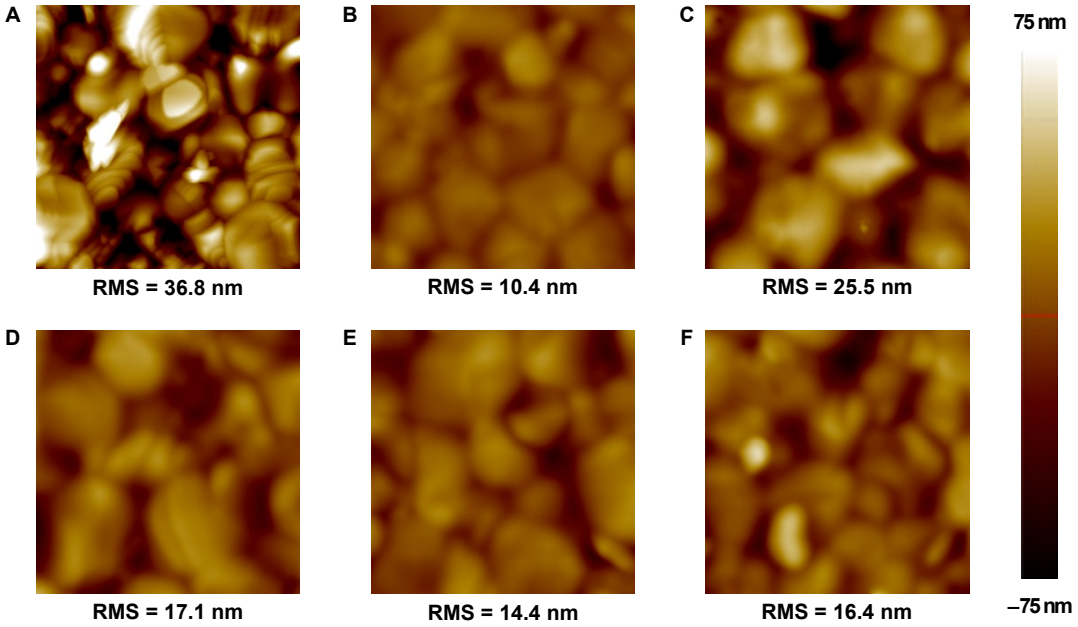

Fig. S19 Atomic force microscopy images for the sample of ITO/SnO_2/perovskite/TTI-derived layer (A) and that covered with an HTL of (B) spiro-OMeTAD, (C) PTAA, (D) p-TPA3Me-E, (E) p-TPA3Me-E-TPAOOD-E, or (F) p-TPAOOD-E. The root mean square (RMS) roughness values are shown below each image. Image size: 5 μm × 5 μm.

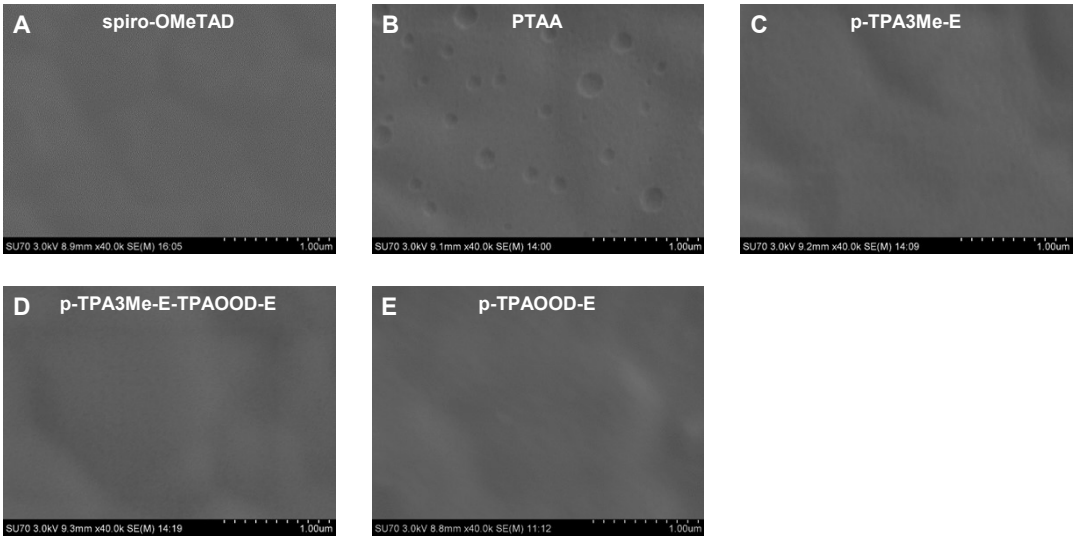

Fig. S20 Top-view scanning electron microscopy images of pristine organic semiconductor layers deposited atop $FAPbI_3$ polycrystalline thin films. Scale bar: 1 μm.

Table S2. Representative photovoltaic parameters of perovskite solar cells with different hole transport layers before and after 1000-hour, 85 °C aging.

Cell	J_{SC} [mA cm^{-2}]	V_{OC} [V]	FF [%]	PCE [%]	J_{SC}^{EQE} [mA cm^{-2}]
spiro-OMeTAD/unaged	26.09	1.185	78.0	24.1	25.77
spiro-OMeTAD/aged	22.83	1.090	65.8	16.4	22.53
p-TPA3Me-E-TPAOOD-E/unaged	26.10	1.185	82.0	25.4	25.78
p-TPA3Me-E-TPAOOD-E/aged	25.53	1.160	77.6	23.0	25.18

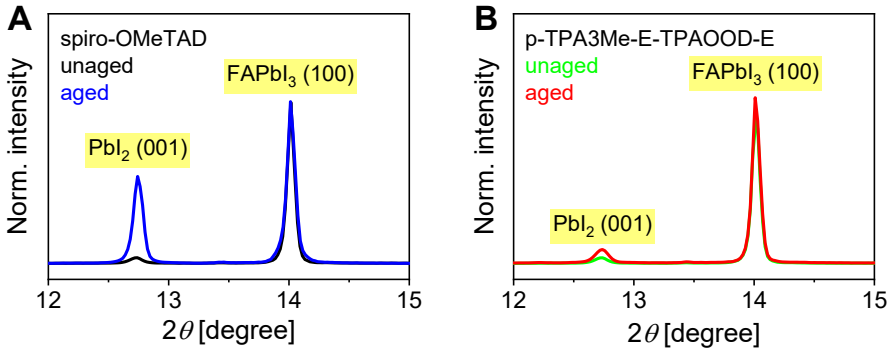

Fig. S21 X-ray diffraction patterns for the unaged and aged cells with spiro-OMeTAD and p-TPA3Me-E-TPAOOD-E.

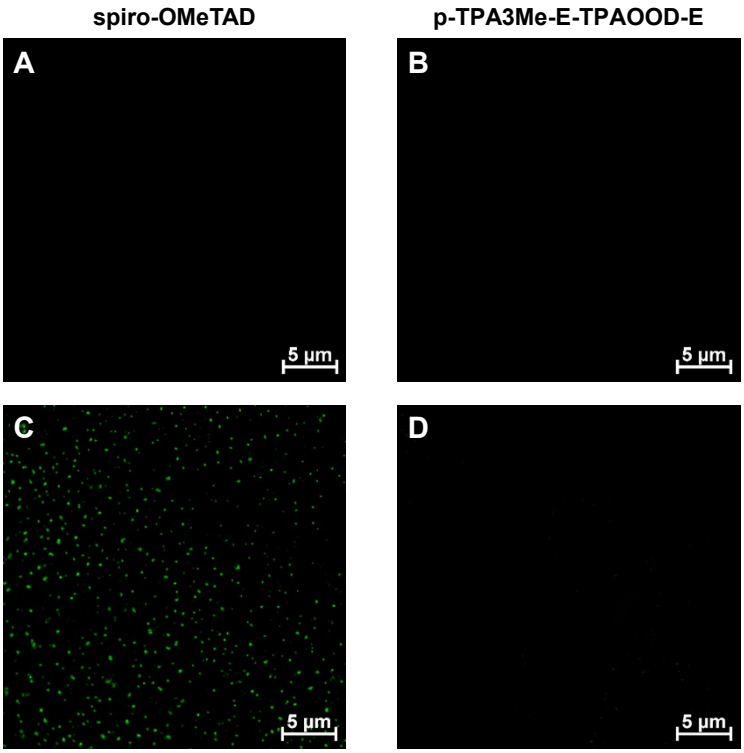

Fig. S22 Fluorescence optical microscopy images of the perovskite layers in (A and B) unaged and (C and D) 85 °C, 1000-hour aged solar cells with different hole transport layers. Scale bar: 5 µm. Prior to measurement, encapsulation materials, gold electrodes, and the hole transport layers were removed.

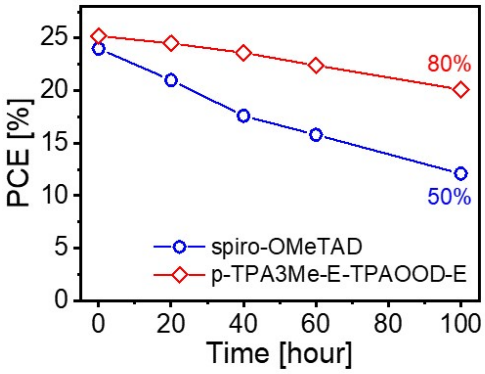

Fig. S23 Power conversion efficiency (PCE) evolution during exposure to a room temperature environment with humidity levels approaching 100%. The data represents average values from four cells.

4 Appendix: ^{1}H NMR spectra, ^{13}C NMR spectra, mass spectra, ATR-FTIR spectra, UV-vis spectra, and HT-GPC analyses

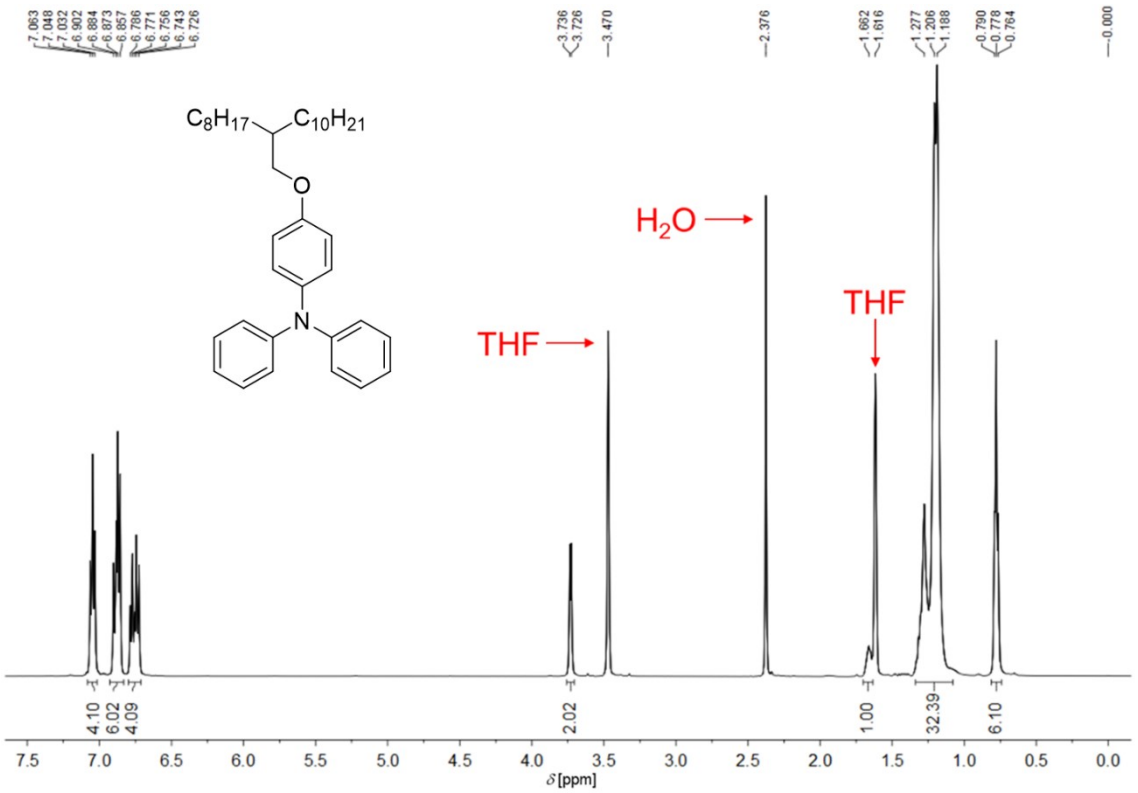

Fig. S24 ^{1}H NMR (400 MHz) spectrum of **TPAOOD** in THF-d_8.

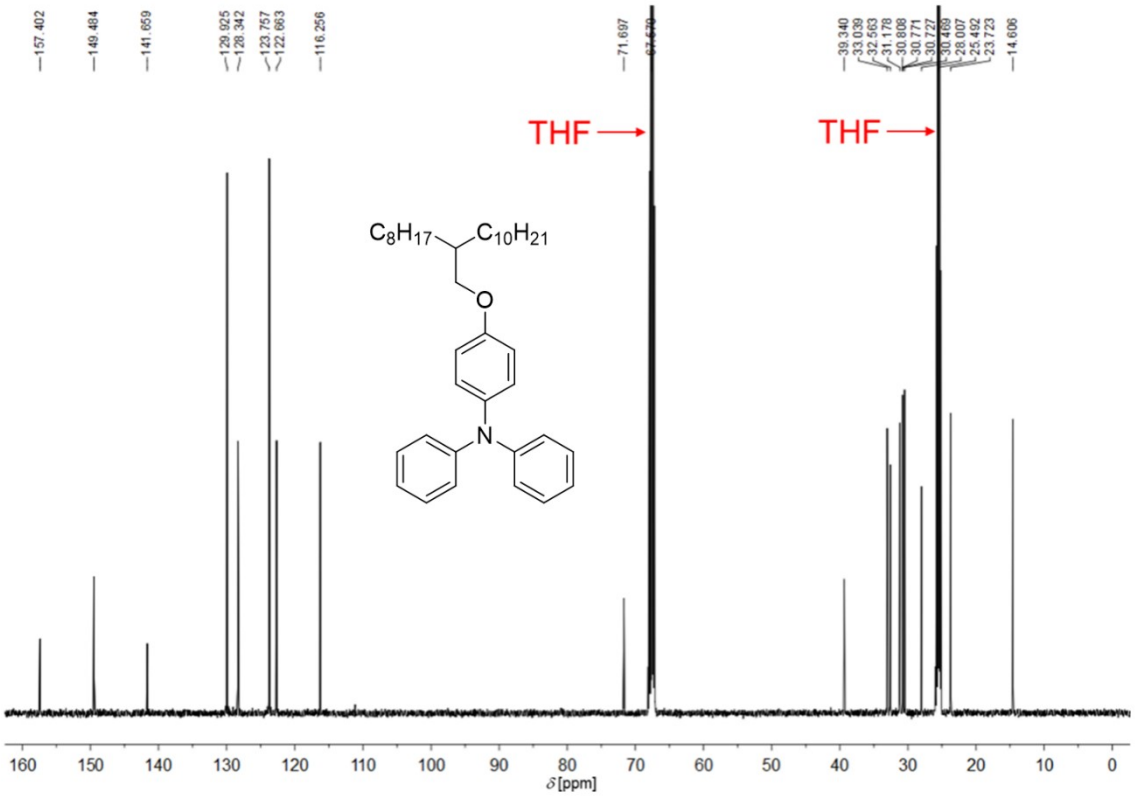

Fig. S25 ^{13}C NMR (100 MHz) spectrum of **TPAOOD** in THF-d_8.

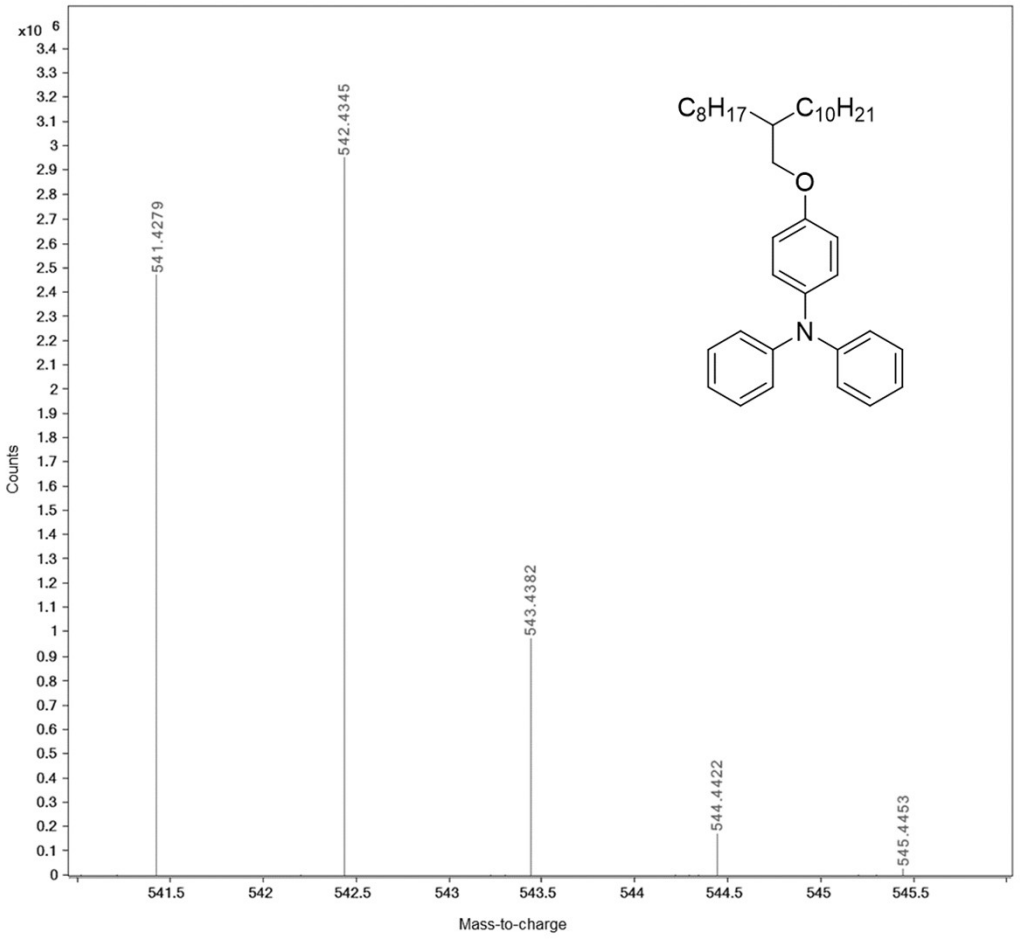

Fig. S26 High-resolution mass spectrum (ESI) of **TPAOOD**.

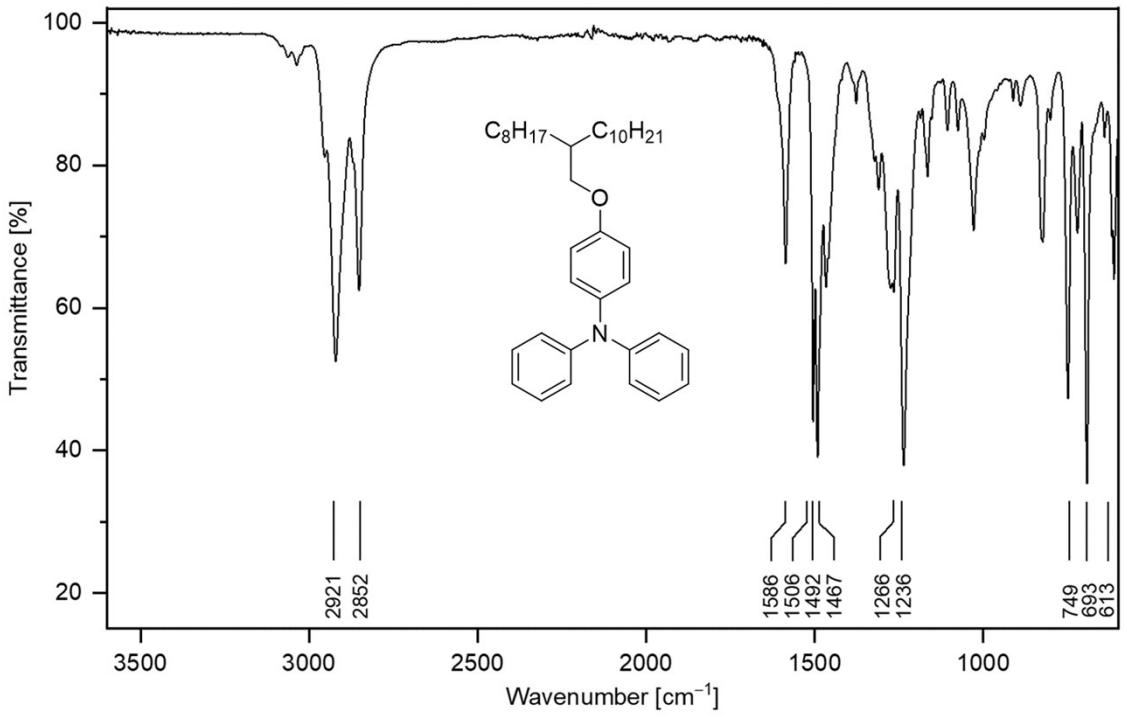

Fig. S27 ATR-FTIR spectrum of **TPAOOD**.

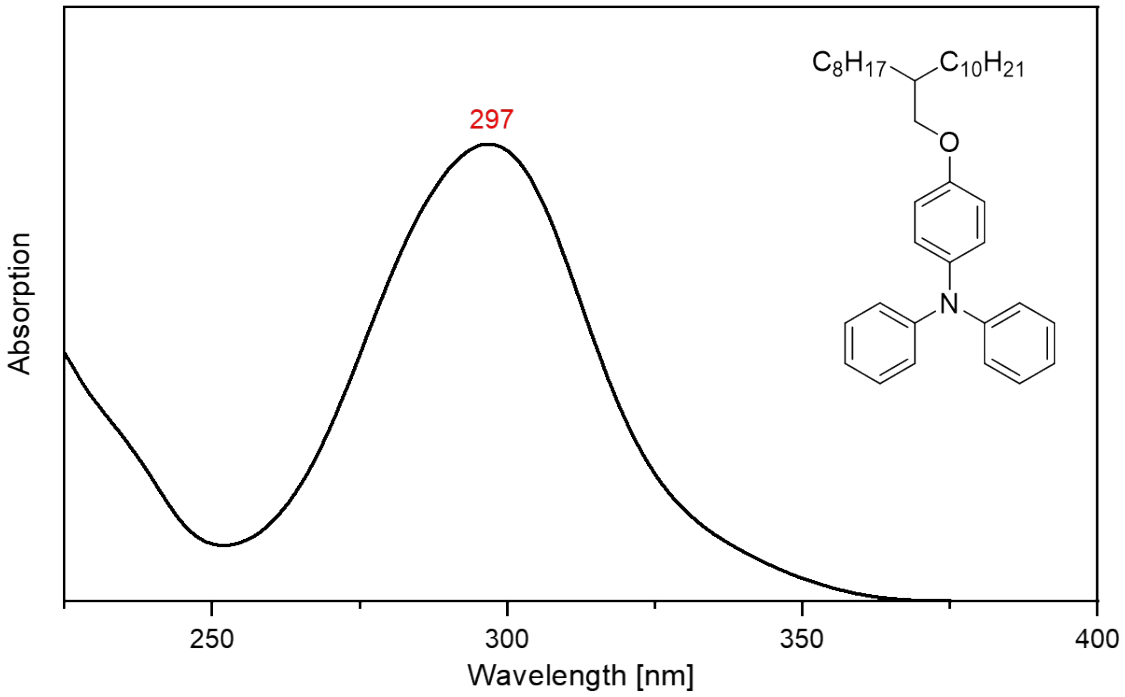

Fig. S28 UV-vis absorption spectrum of **TPAOOD** in THF.

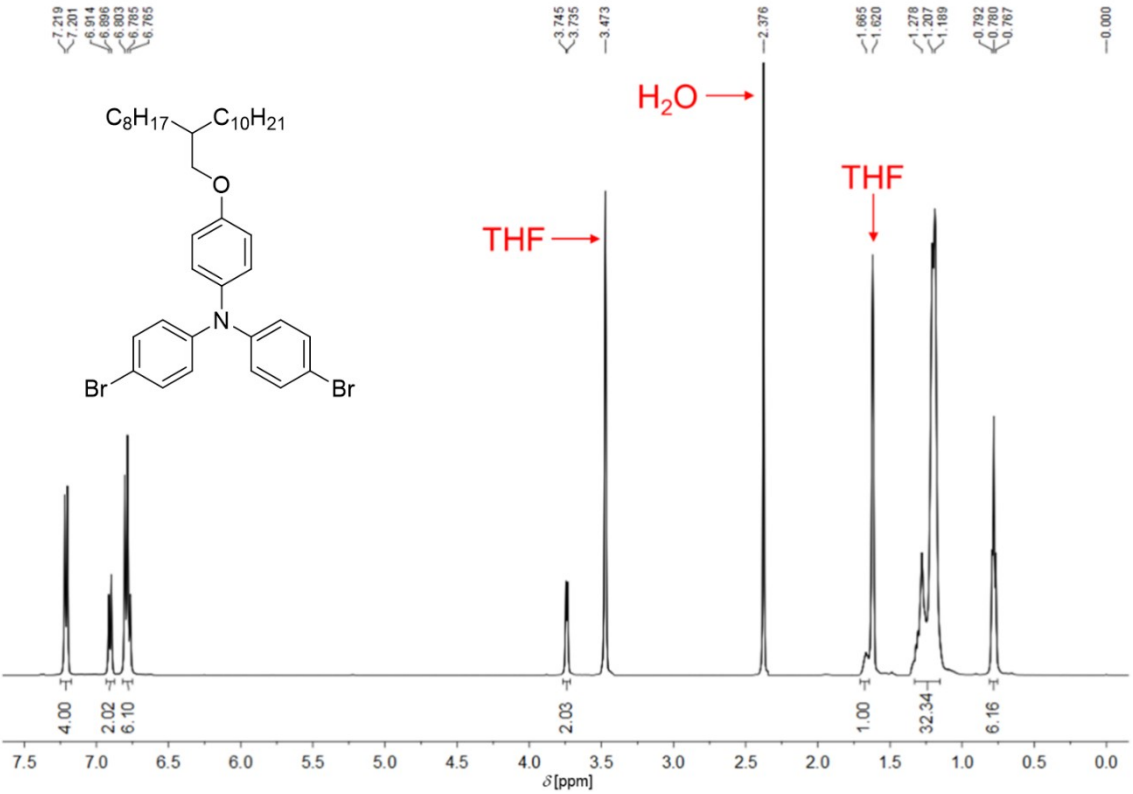

Fig. S29 ^{1}H NMR (400 MHz) spectrum of **2Br-TPAOOD** in THF-d_8.

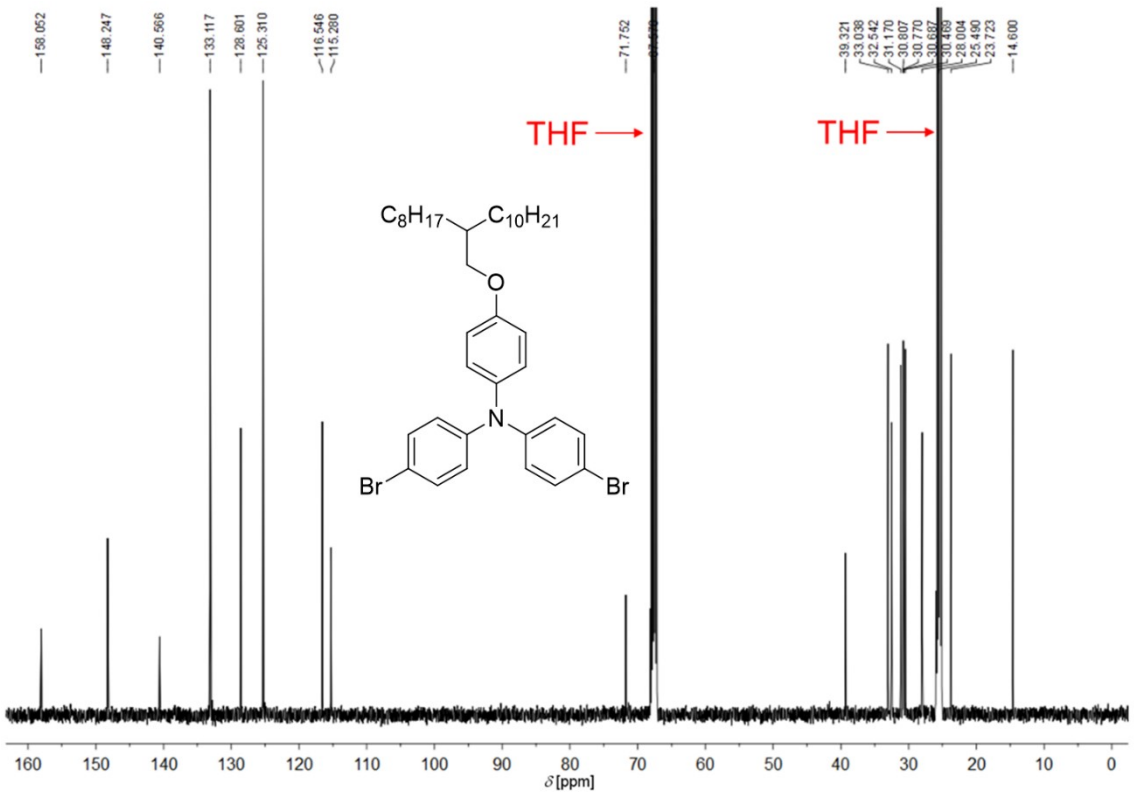

Fig. S30 ^{13}C NMR (100 MHz) spectrum of **2Br-TPAOOD** in THF-d_8.

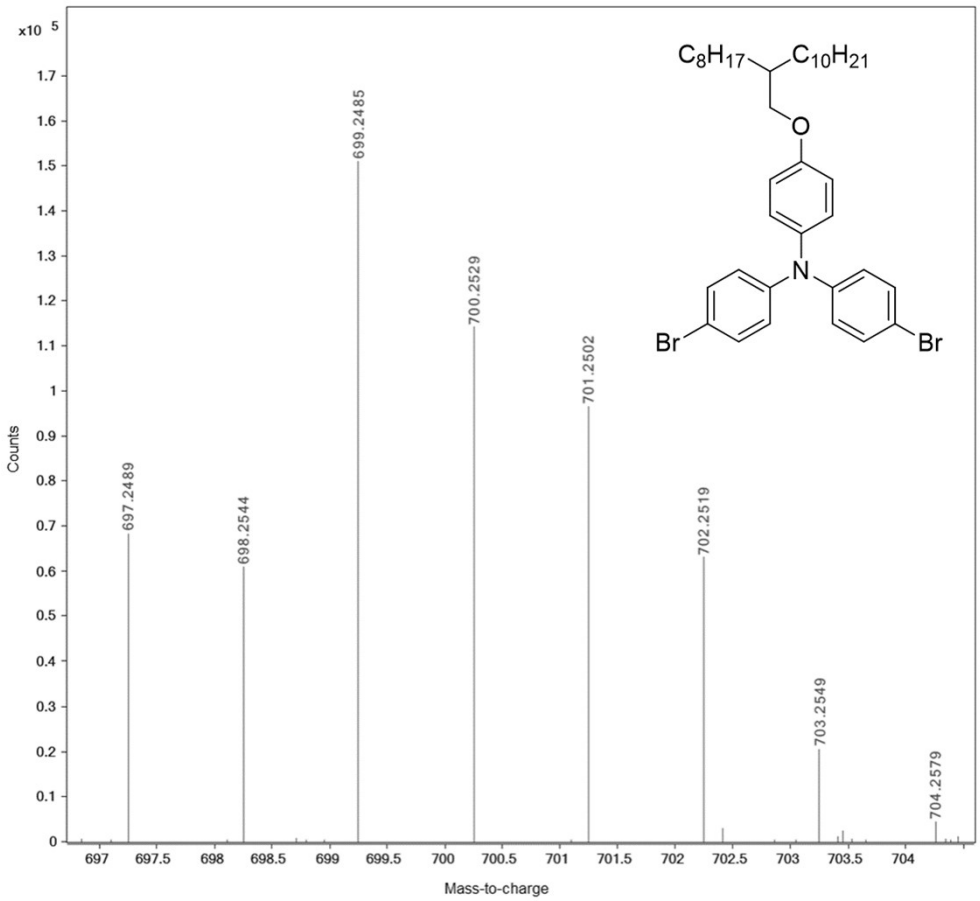

Fig. S31 High-resolution mass spectrum (ESI) of **2Br-TPAOOD**.

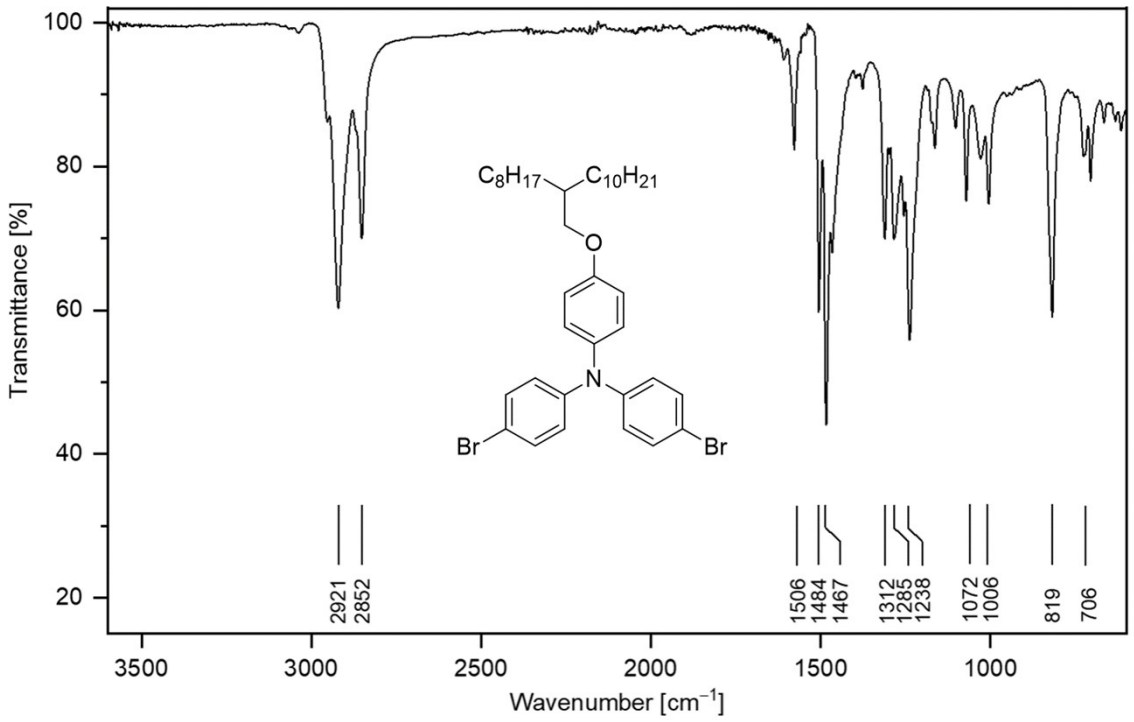

Fig. S32 ATR-FTIR spectrum of **2Br-TPAOOD**.

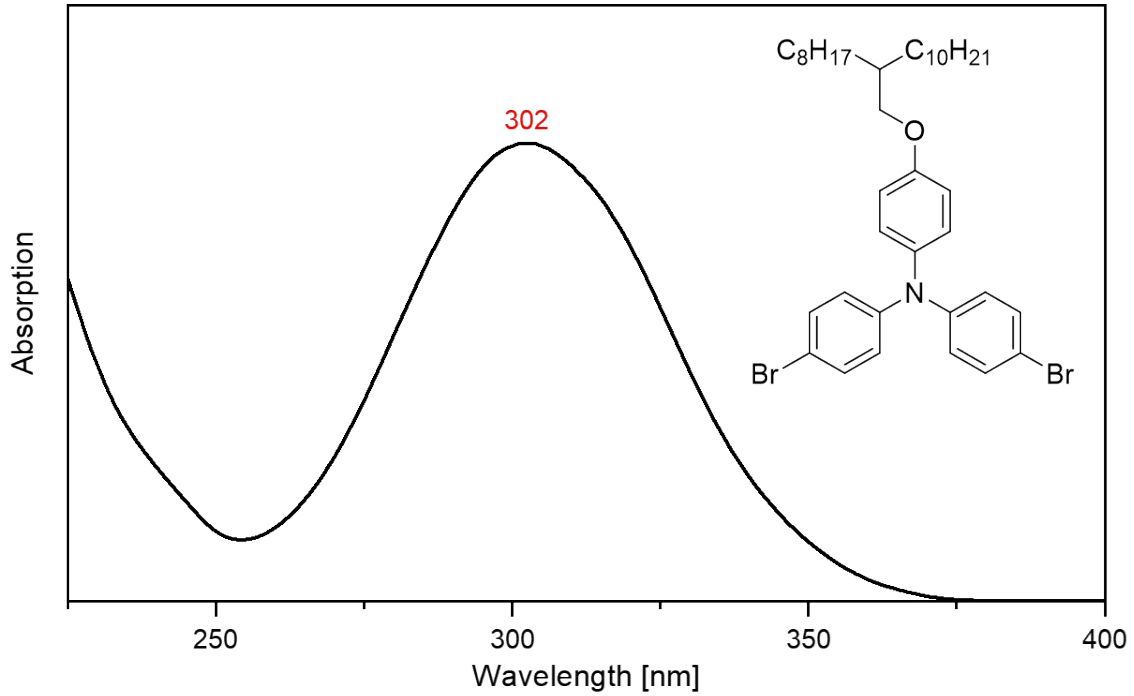

Fig. S33 UV-vis absorption spectrum of **2Br-TPAOOD** in THF.

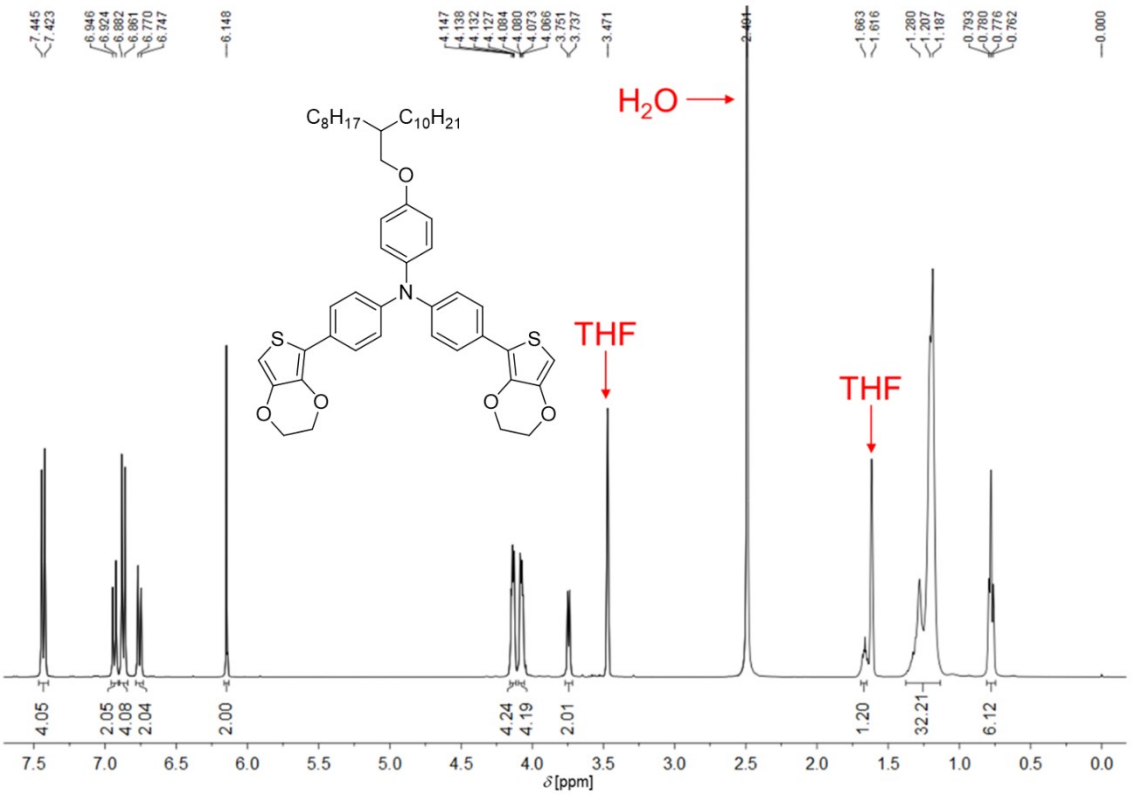

Fig. S34 ^{1}H NMR (400 MHz) spectrum of **E-TPAOOD-E** in THF-d_8.

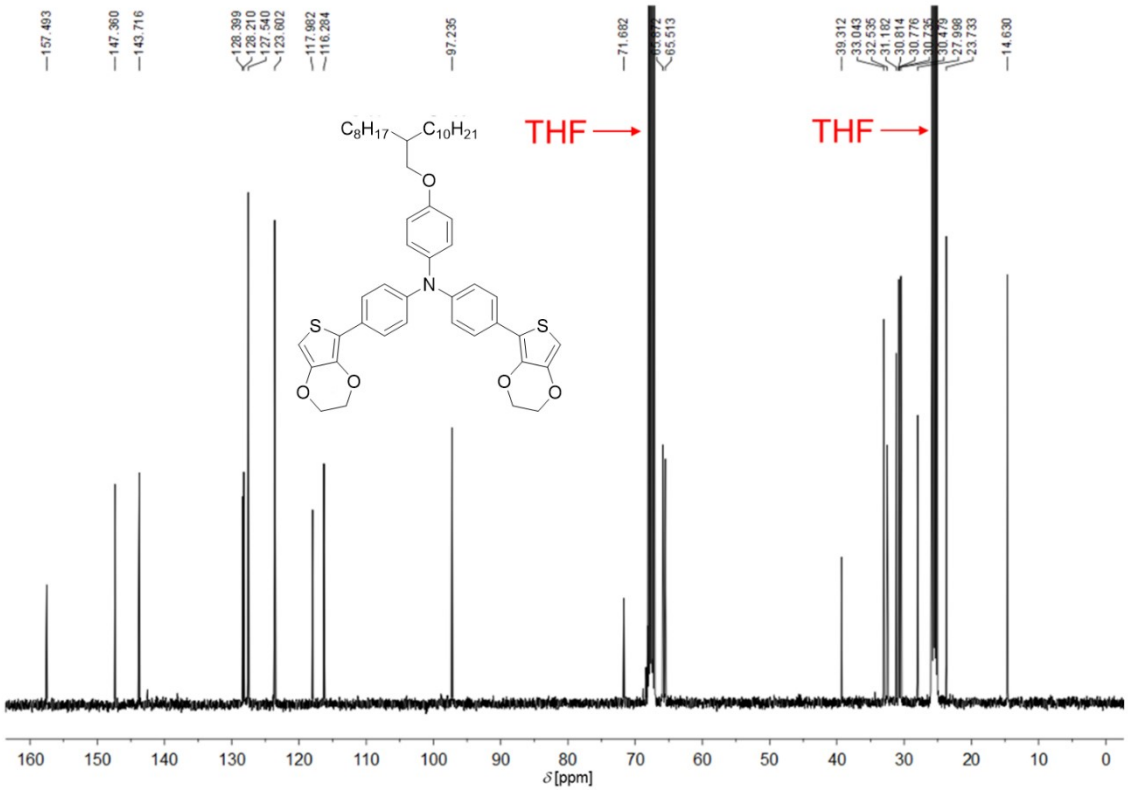

Fig. S35 ^{13}C NMR (100 MHz) spectrum of **E-TPAOOD-E** in THF-d_8.

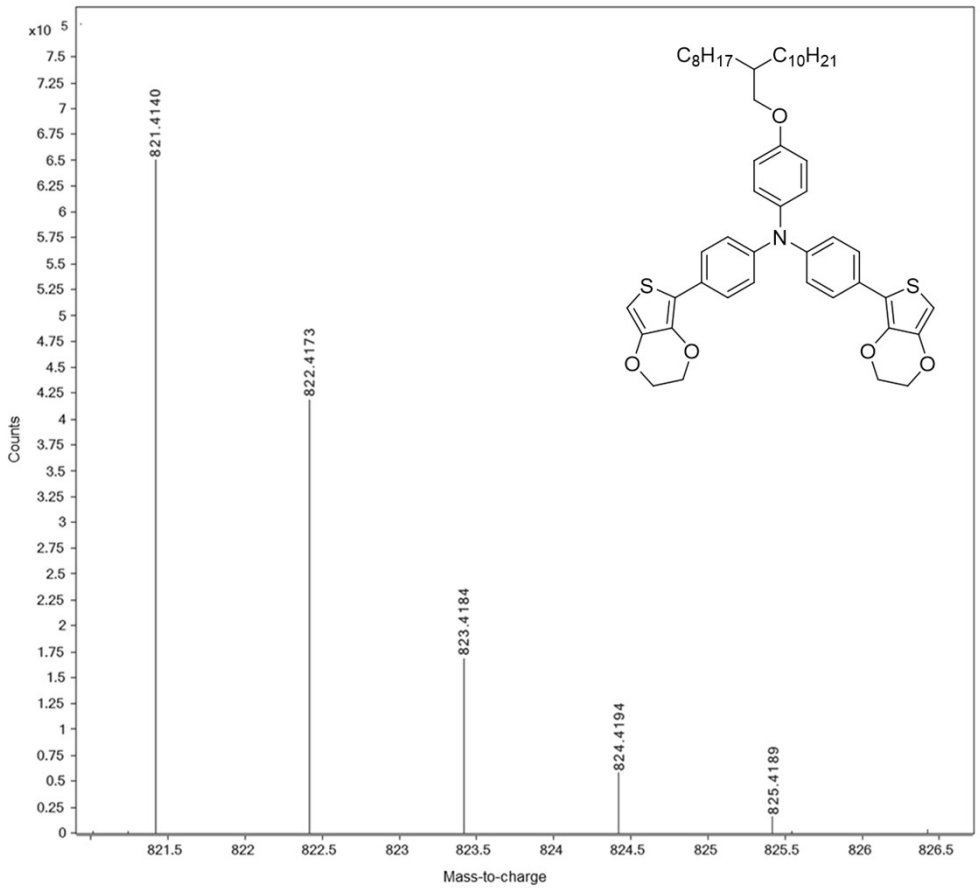

Fig. S36 High-resolution mass spectrum (ESI) of **E-TPAOOD-E**.

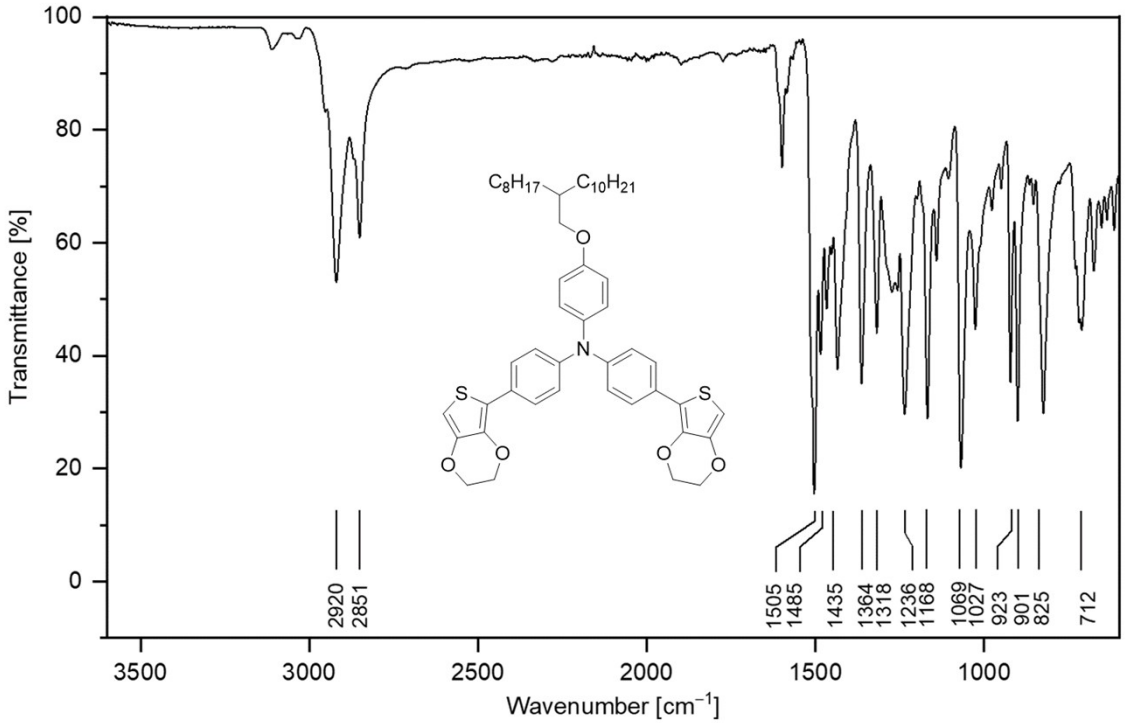

Fig. S37 ATR-FTIR spectrum of **E-TPAOOD-E**.

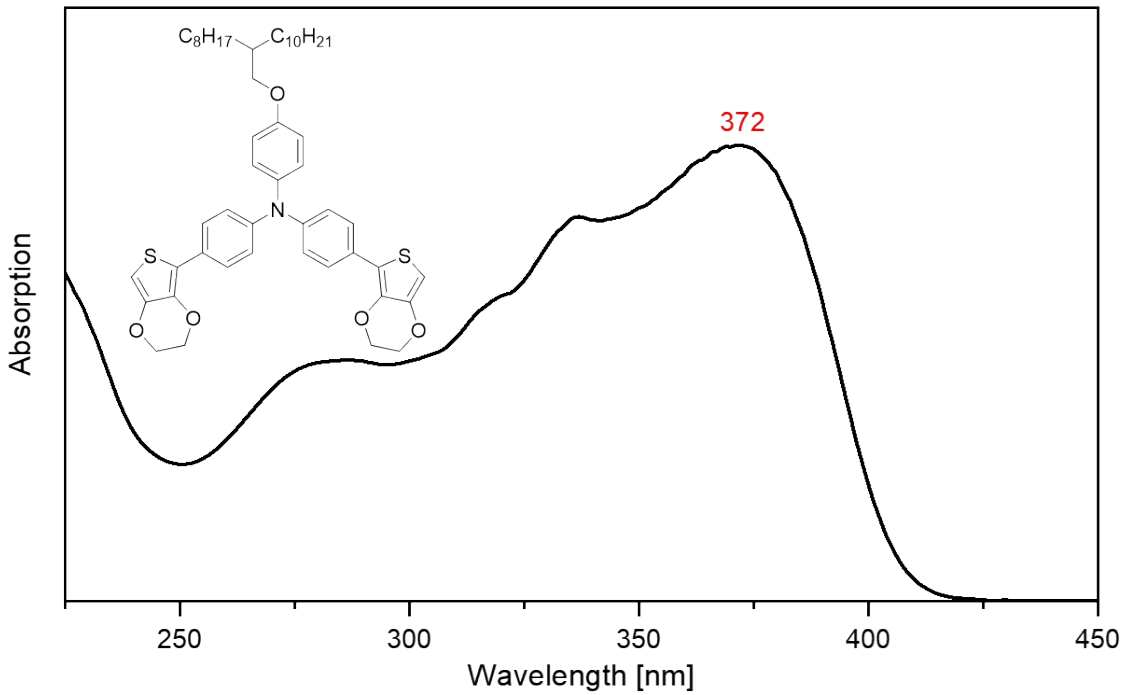

Fig. S38 UV-vis absorption spectrum of **E-TPAOOD-E** in THF.

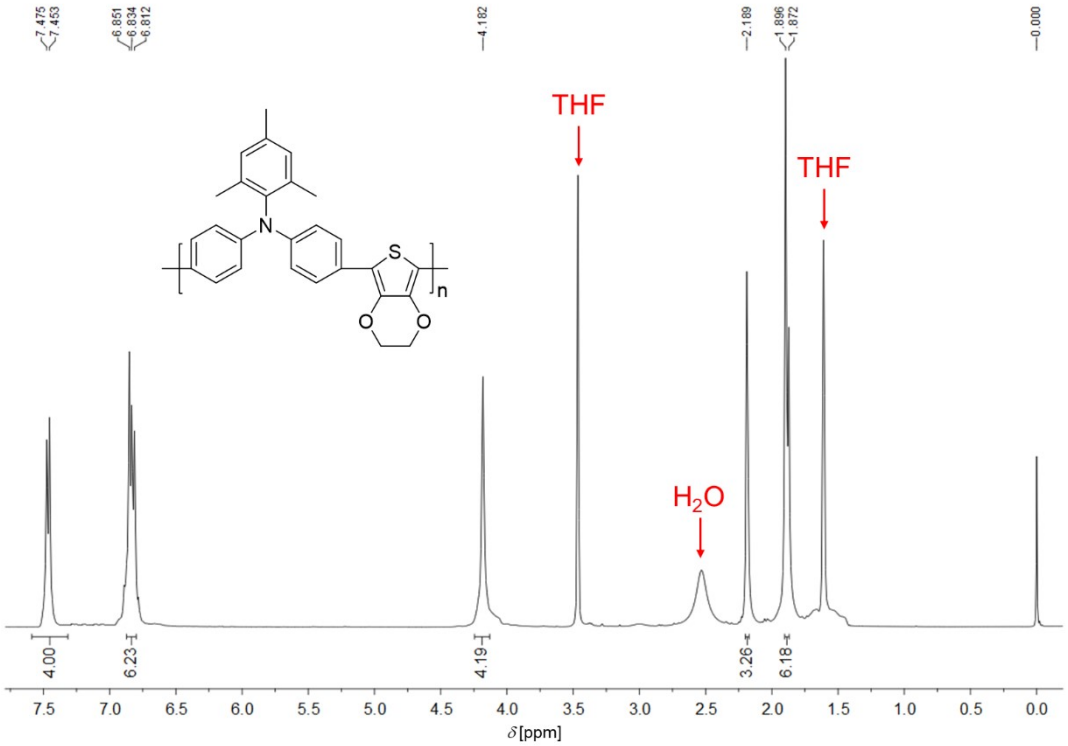

Fig. S39 ^{1}H NMR (400 MHz) spectrum of **p-TPA3Me-E** in THF-d_8.

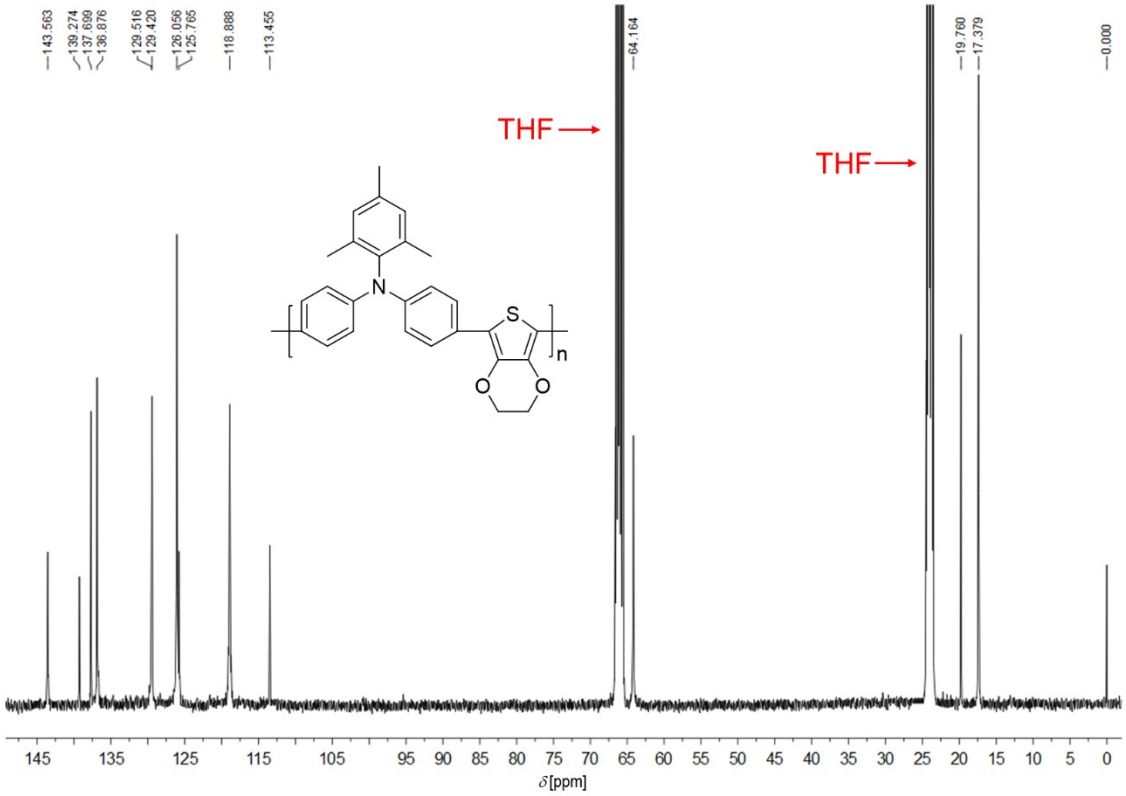

Fig. S40 ^{13}C NMR (100 MHz) spectrum of **p-TPA3Me-E** in THF-d_8.

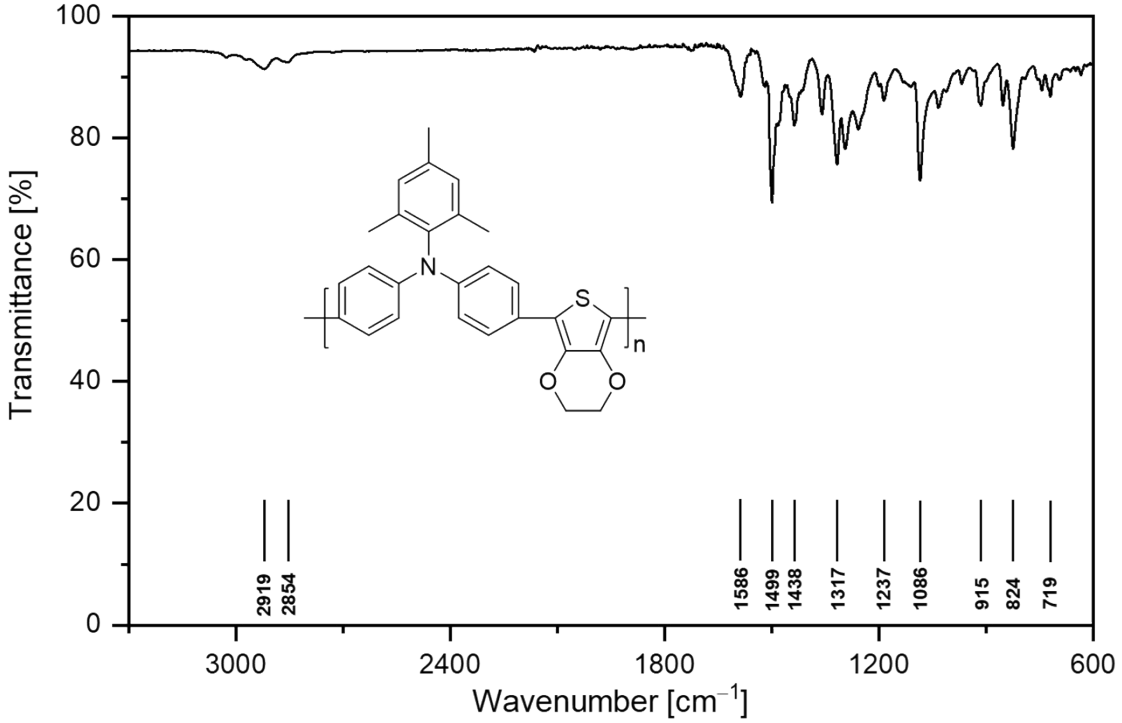

Fig. S41 ATR-FTIR spectrum of **p-TPA3Me-E**.

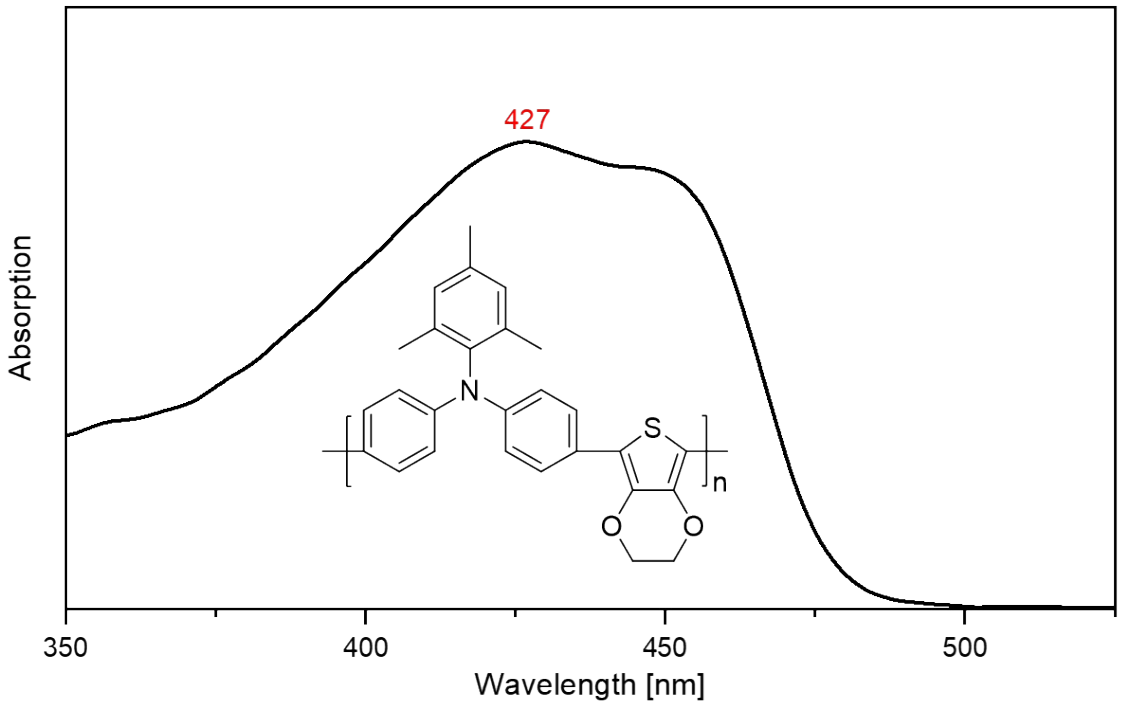

Fig. S42 UV-vis spectrum of **p-TPA3Me-E**.

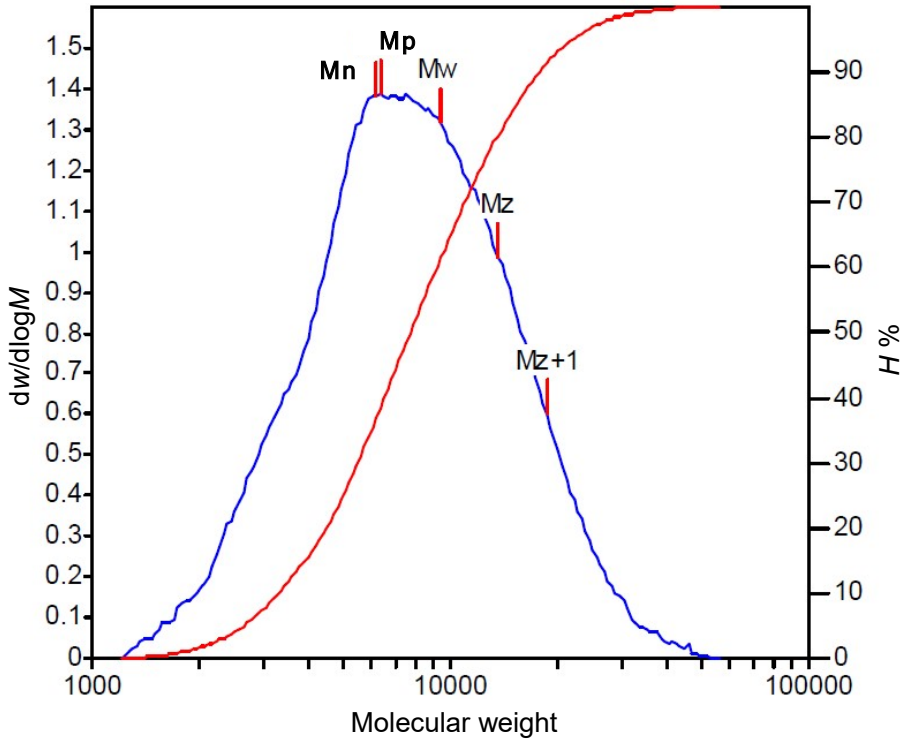

Fig. S43 Molecular weight distribution plot of **p-TPA3Me-E**. The d*w*/dlog*M* plot is represented by the blue solid line, and the cumulative plot is depicted by the red solid line.

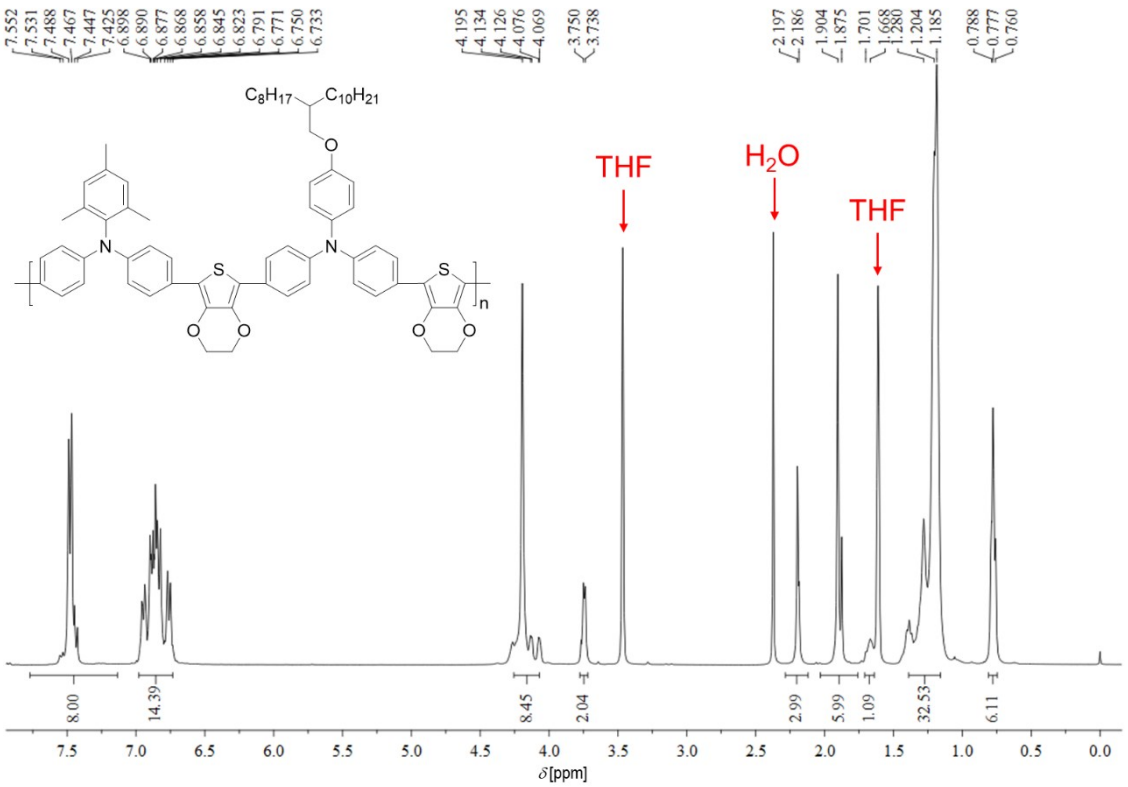

Fig. S44 ^{1}H NMR (400 MHz) spectrum of **p-TPA3Me-E-TPAOOD-E** in THF-d_8.

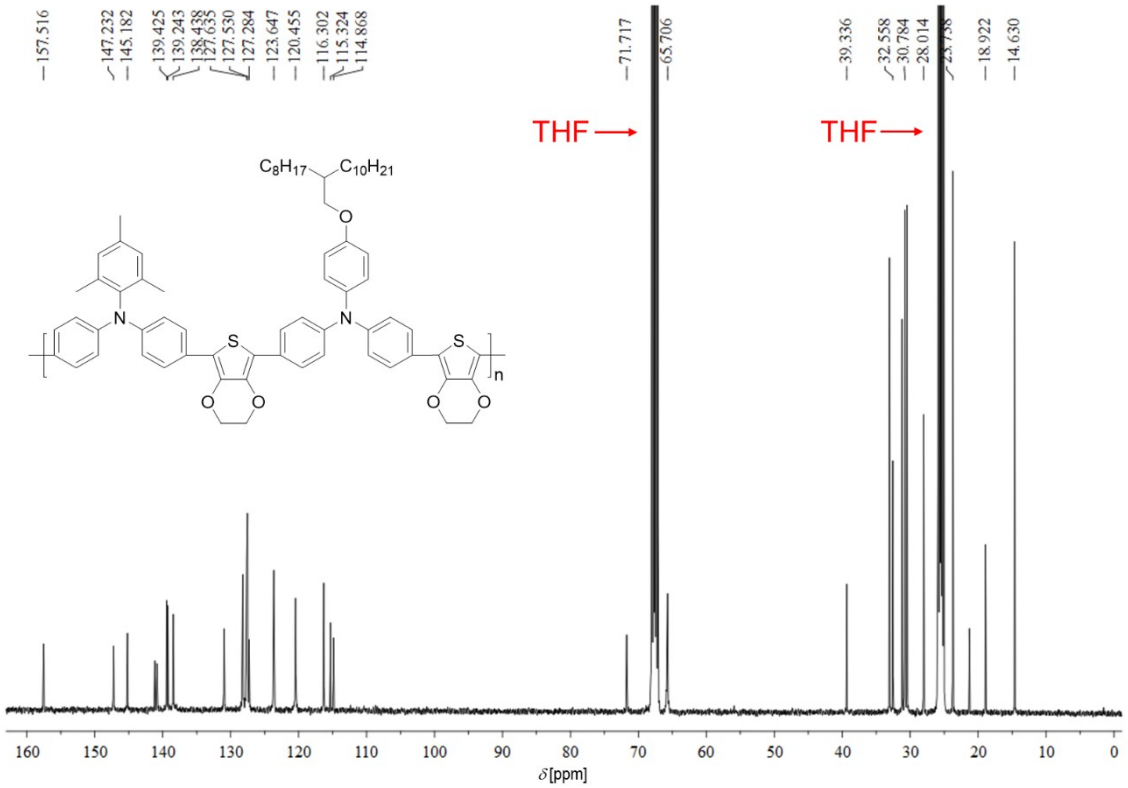

Fig. S45 ^{13}C NMR (100 MHz) spectrum of **p-TPA3Me-E-TPAOOD-E** in THF-d_8.

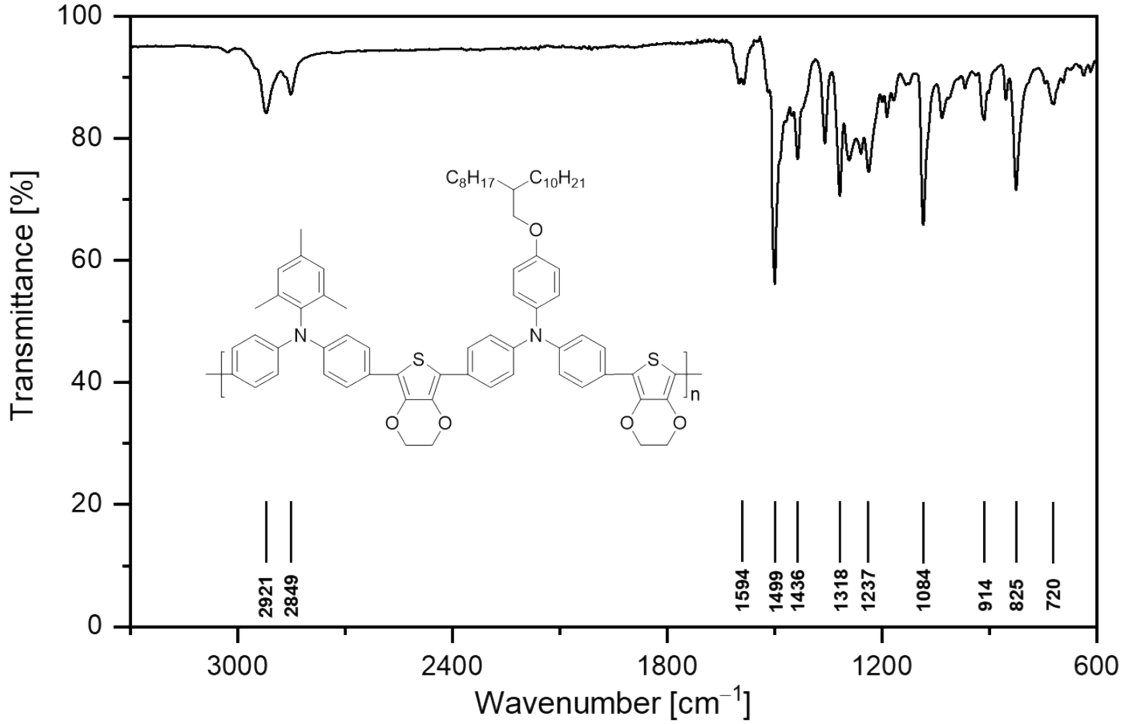

Fig. S46 ATR-FTIR spectrum of **p-TPA3Me-E-TPAOOD-E**.

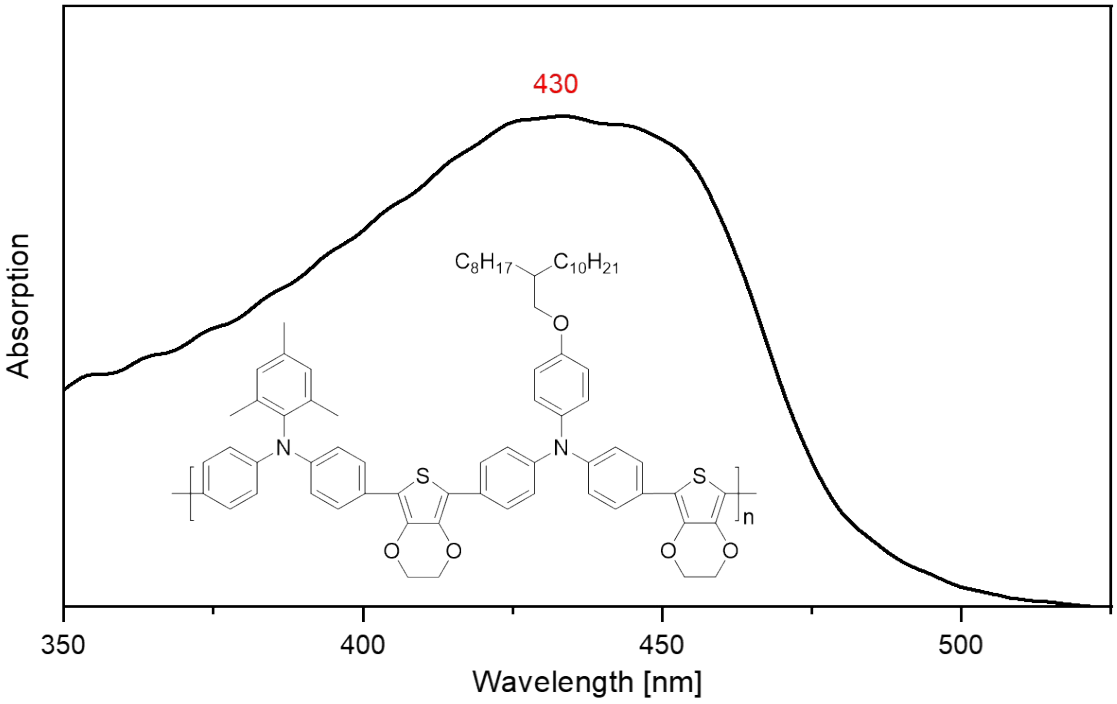

Fig. S47 UV-vis spectrum of **p-TPA3Me-E-TPAOOD-E**.

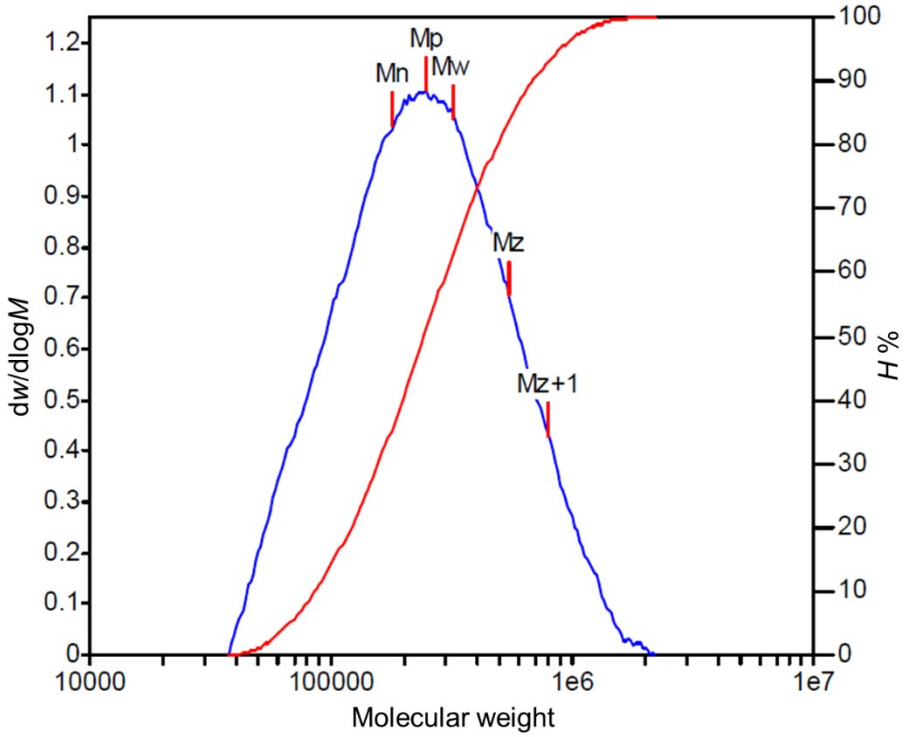

Fig. S48 Molecular weight distribution plot of **p-TPA3Me-E-TPAOOD-E**. The d*w*/dlog*M* plot is represented by the blue solid line, and the cumulative plot is depicted by the red solid line.

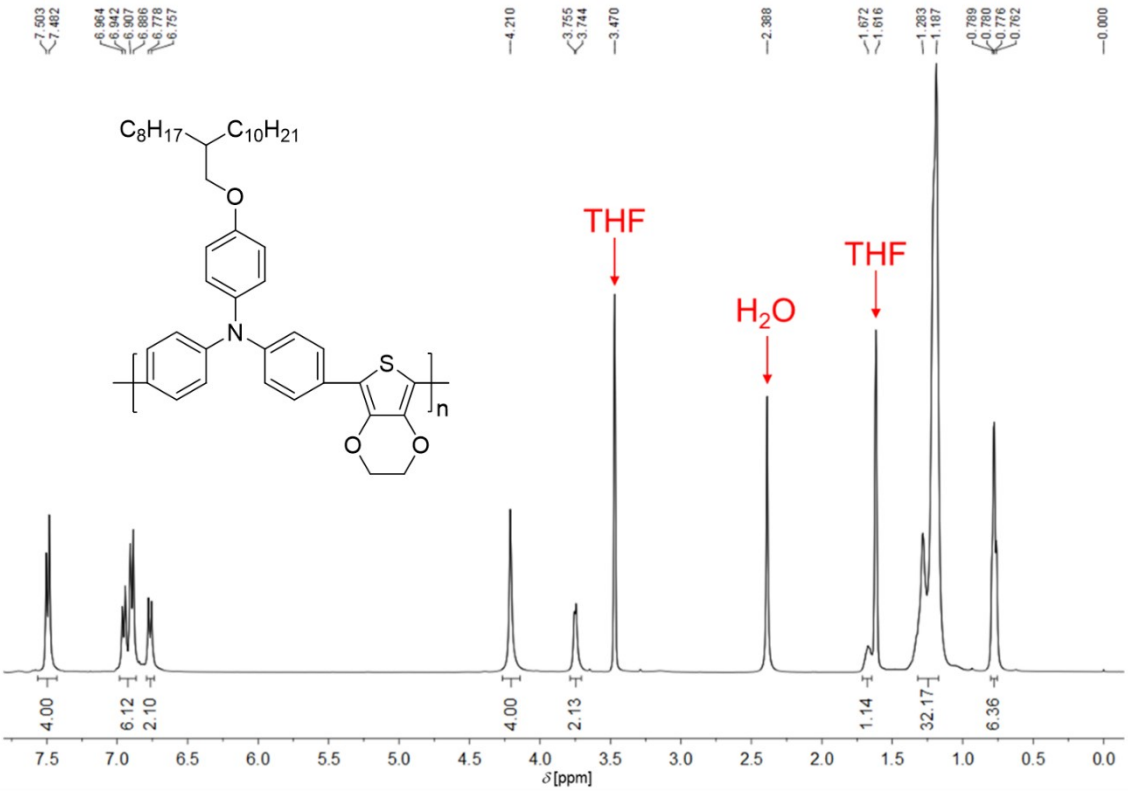

Fig. S49 ^{1}H NMR (400 MHz) spectrum of **p-TPAOOD-E** in THF-d_8.

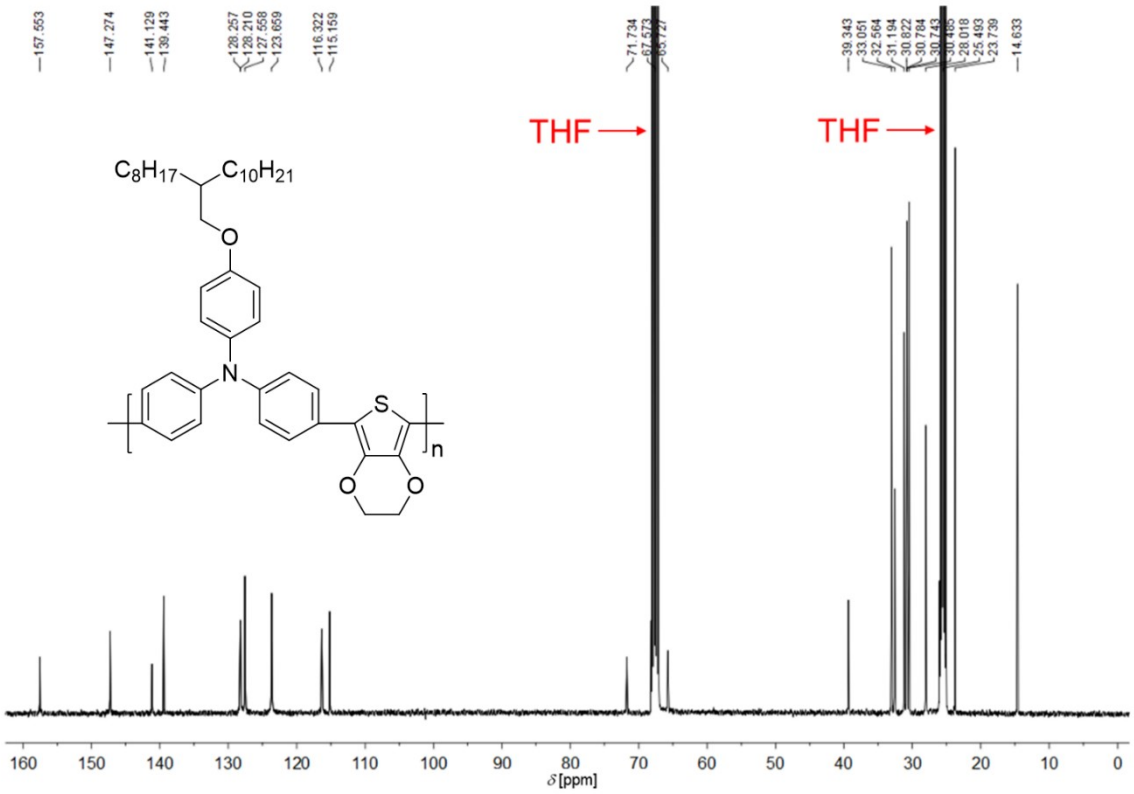

Fig. S50 ^{13}C NMR (100 MHz) spectrum of **p-TPAOOD-E** in THF-d_8.

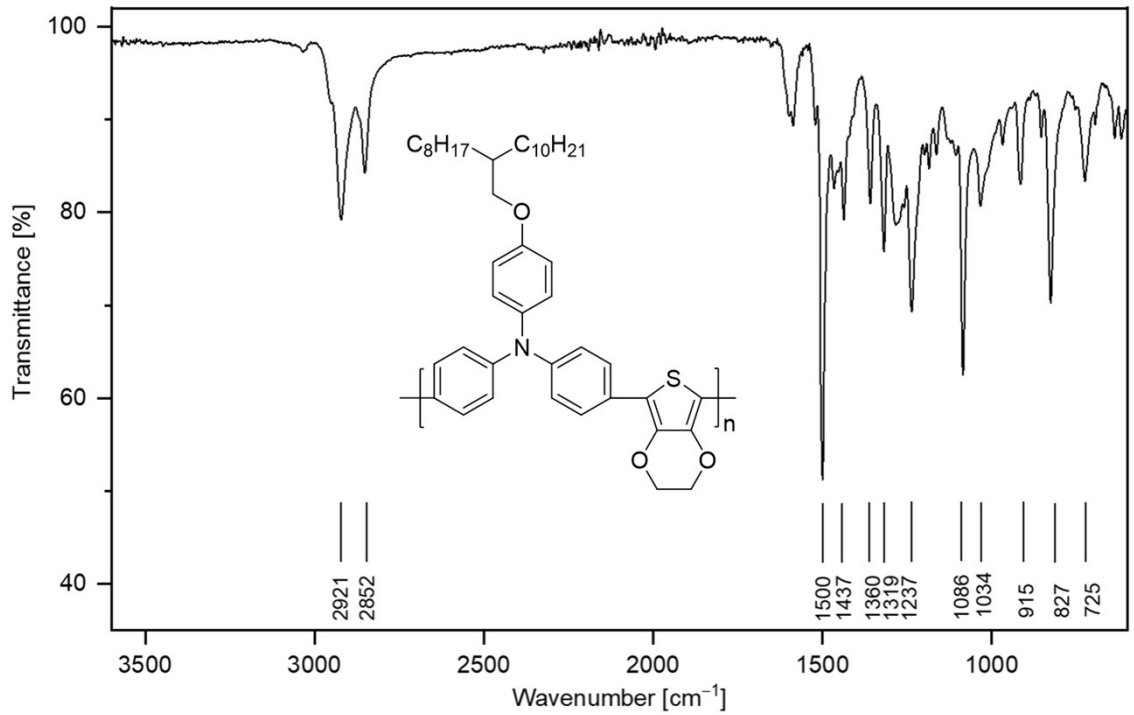

Fig. S51 ATR-FTIR spectrum of **p-TPAOOD-E**.

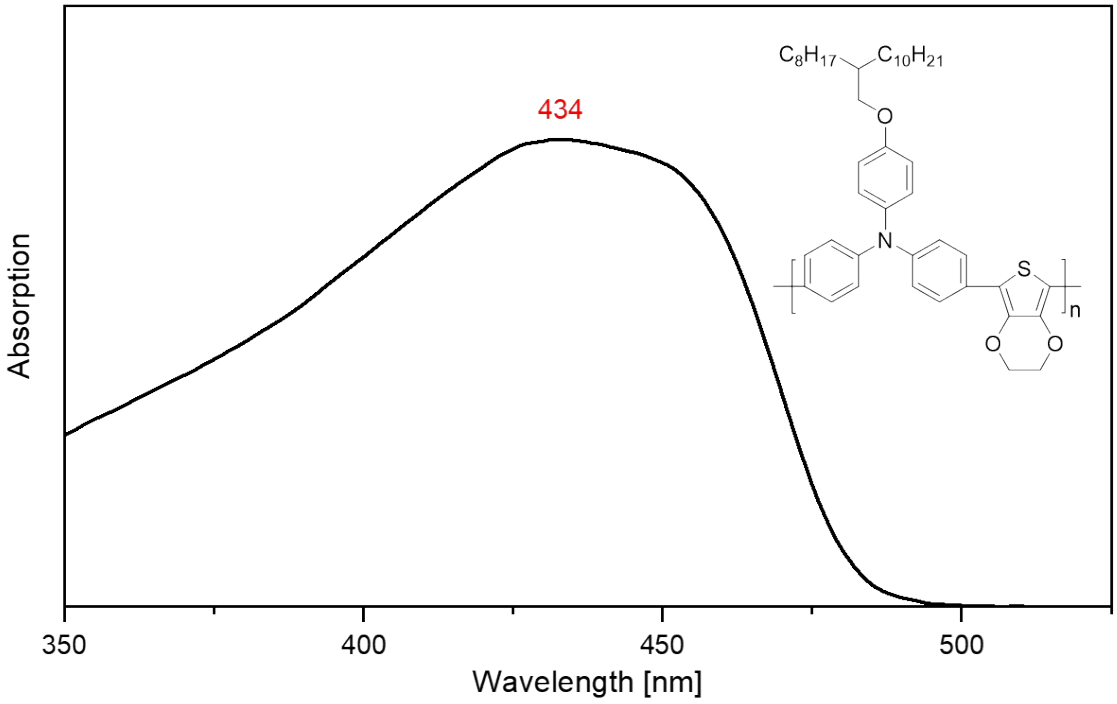

Fig. S52 UV-vis spectrum of **p-TPAOOD-E**.

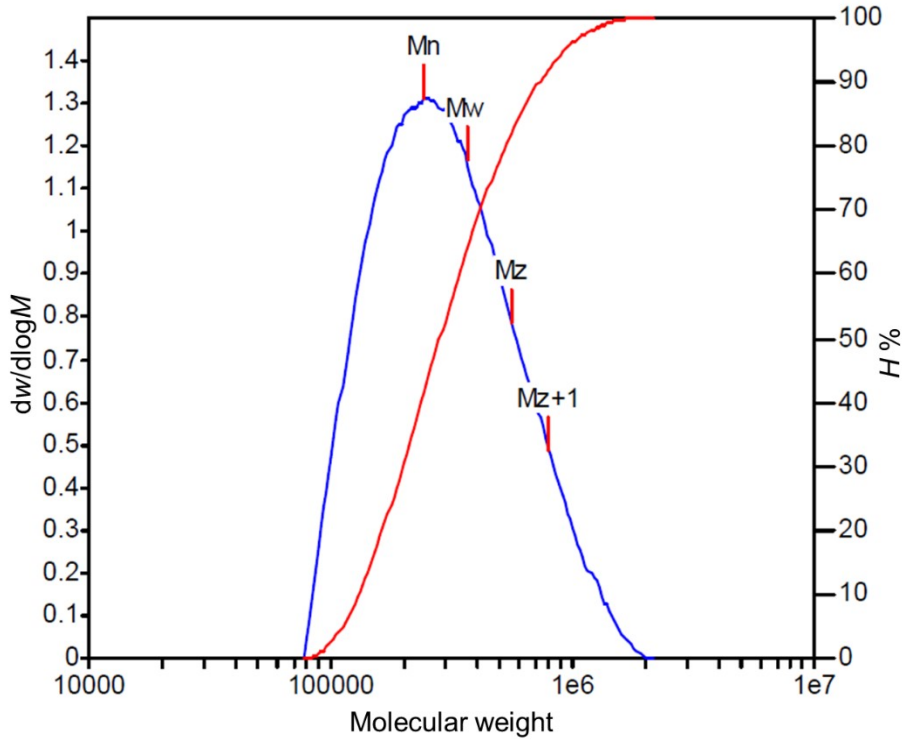

Fig. S53 Molecular weight distribution plots of **p-TPAOOD-E**. The d*w*/dlog*M* plot is represented by the blue solid line, and the cumulative plot is depicted by the red solid line.

5 References

1 Y. Kim, E. H. Jung, G. Kim, D. Kim, B. J. Kim and J. Seo, *Adv. Energy Mater.*, 2018, **8**, 1801668.

2 M. C. Hwang, H. Kang, K. Yu, H.-J. Yun, S.-K. Kwon, K. Lee and Y.-H. Kim, *Sol. Energ. Mat. Sol. C.*, 2014, **125**, 39.

3 M. M. Tepliakova, A. V. Akkuratov, S. A. Tsarev and P. A. Troshin, *Tetrahedron Lett.*, 2020, **61**, 152317.

4 T. Li, Y. Zhang, M. Ren, Y. Mu, J. Zhang, Y. Yuan, M. Zhang and P. Wang, *Angew. Chem. Int. Ed.*, 2024, **63**, e202401604.

5 Y. Zhao, F. Ma, Z. Qu, S. Yu, T. Shen, H.-X. Deng, X. Chu, X. Peng, Y. Yuan, X. Zhang and J. You, *Science*, 2022, **377**, 531.

6 Q. Jiang, Y. Zhao, X. Zhang, X. Yang, Y. Chen, Z. Chu, Q. Ye, X. Li, Z. Yin and J. You, *Nat. Photonics*, 2019, **13**, 460.

7 L. He, Y. Zhang, Y. Wei, Y. Cai, J. Zhang and P. Wang, *Matter*, 2023, **6**, 4013.

8 C. M. Cardona, W. Li, A. E. Kaifer, D. Stockdale and G. C. Bazan, *Adv. Mater.*, 2011, **23**, 2367.